FROM FUNDAMENTAL FULLERENES TO THE CARDINAL CALCIUM CANDIDATE: THE DEVELOPMENT OF A LASER ABLATION ION SOURCE AND ITS DIVERSE APPLICATION AT THE LEBIT FACILITY

By

Scott Edward Bustabad

A DISSERTATION

Submitted to
Michigan State University
in partial fulfillment of the requirements
for the degree of

Physics - Doctor of Philosophy

2014

ABSTRACT

FROM FUNDAMENTAL FULLERENES TO THE CARDINAL CALCIUM CANDIDATE: THE DEVELOPMENT OF A LASER ABLATION ION SOURCE AND ITS DIVERSE APPLICATION AT THE LEBIT FACILITY

By

Scott Edward Bustabad

A Laser Ablation Source (LAS) has been developed at the Low Energy Beam and Ion Trap (LEBIT) mass spectrometry facility at the National Superconducting Cyclotron Laboratory. LAS enhances the offline capability of LEBIT providing increased access to ions for measurements of scientific interest as well as for calibration measurements and checks of systematic effects. The design and implementation of LAS are described in this work.

Carbon cluster ions produced via laser ablation were used to probe LEBIT mass-dependent systematic effects. Since carbon cluster ions span the entire nuclear chart and have essentially no mass uncertainty, they are the ideal tool for these studies. As part of this thesis work, frequency shifts across a 108 u mass range were quantified and found to lead to a relative error in mass determination less than 10^{-9}/u.

LAS was operated in tandem with the surface ion source to produce ions of $^{48}Ca^{+}$ and $^{48}Ti^{+}$ for the first direct measurement of the ^{48}Ca double beta decay Q value. Accurate knowledge of this Q value is important for experiments that employ ^{48}Ca for neutrinoless double beta decay searches. The LEBIT high precision Penning trap Q value measurement revealed a 3 σ shift from the previously accepted value and reduced the uncertainty by a factor of five. The measurement procedure and results are discussed in this thesis.

The first direct determination of the ^{78}Kr double electron Q value was accomplished at the LEBIT facility. This determination indicates a 2 σ shift from the previously accepted value

and reduces the uncertainty by a factor of three. With the improved Q value determination, the resonance condition was explored for various double electron captures. The potential for resonance enhancement is evaluated, and the viability of ^{78}Kr as a candidate for neutrinoless double electron capture experiments is discussed.

TABLE OF CONTENTS

LIST OF TABLES

LIST OF FIGURES

Chapter 1

Introduction

1.1 Motivation for the development of a laser ion source

The Low Energy Beam and Ion Trap facility at the National Superconducting Cyclotron Laboratory provides high precision Penning trap measurements of atomic masses. Increased access to ions of stable and long-lived isotopes via simple offline production methods would enhance the capabilities of the LEBIT facility. With a wide array of stable, well known masses available, detailed checks of the experimental apparatus and an evaluation of systematic effects can be performed; see for example [1, 2, 3]. The results of these types of measurements can even be used to minimize systematic effects in the future.

In addition, having access to well known masses throughout a broad mass range is important for ensuring that good reference masses are available during measurements; see Section 2.5.5. Having a nearby, well known reference ion is an integral part of performing a reliable, high precision measurement because of two primary reasons: first, systematic effects scale approximately linearly with the mass difference between the ion of interest and the reference ion; second, the uncertainty of the reference ion contributes to the uncertainty of the measurement [4].

Finally, a variety of offline ion production methods helps maximize the scientific output of the LEBIT facility. In addition to radioactive beam experiments, increased offline capabilities

enable LEBIT to perform key mass measurements of stable and long-lived isotopes of interest. Given the need for ions of stable and long-lived isotopes, it was proposed to develop a new offline ion source that would complement the existing offline ion sources. The development and application of the laser ablation source (LAS) at LEBIT is the central work of this thesis.

1.2 Penning trap mass measurements that impact neutrino physics

The primary mass measurements of scientific interest of this thesis work are relevant to particle, weak interaction, and neutrino physics. In the last 15 years, Penning trap atomic mass measurements of candidate isotopes for neutrinoless double electron capture and double beta decay experiments have been used to determine the energy release, i.e. the Q value, of these decays. Accurate knowledge of the Q value for one of these reactions is vital to help determine the decay rate and to identify precisely the location of the zero neutrino peak in the decay spectrum. This section introduces double electron capture and double beta decay, provides an overview of the Penning trap measurements of candidate isotopes, and discusses the opportunity and motivation for the first direct measurements of the ^{78}Kr double electron capture Q value and the ^{48}Ca double beta decay Q value.

1.2.1 Double electron capture

1.2.1.1 Introduction

Proton rich nuclei can in general decay towards the valley of stability through electron capture. In this process, an atomic electron e is captured, a proton p in the nucleus is

converted to a neutron n, and a electron neutrino ν_e is emitted:

$$p + e \longrightarrow n + \nu_e \text{ (occurs in a nucleus)} \tag{1.1}$$

Half-lives for electron captures range from fractions of a second to thousands of years. Similar to single electron capture, proton rich nuclei can also capture two atomic electrons converting two protons into neutrons and releasing two electron neutrinos. These so called double electron capture, ECEC, processes have very long half-lives, $\sim 10^{21}$ years, and are thus typically drowned out by more dominant decay modes. There are, however, 34 proton-rich, even-even nuclei (i.e. nuclei with an even number of protons and an even number of neutrons) that can only decay through two-nucleon processes like double electron capture [5]. For these nuclei, pairing effects cause single electron capture to neighboring odd-odd nuclei to be energetically forbidden. For example, as can be seen in Figure 1.1, barium-130 can not single electron capture to cesium-130, but double electron capture to xenon-130 is possible:

$$^{130}\text{Ba} \longrightarrow ^{130}\text{Xe} + 2\nu_e, \tag{1.2}$$

where ^{130}Ba and ^{130}Xe represent atomic barium-130 and atomic xenon-130 respectively. The two neutrino ECEC in ^{130}Ba has been observed experimentally and a half-life of (2.2 $\pm$ 0.5)$\times$ 10^{21} years has been measured [6].

1.2.1.2 Neutrinoless double electron capture and resonance enhancement

If neutrinos are their own antiparticles, i.e. they are Majorana particles, then the two neutrinos in double electron capture could annihilate in a so-called zero-neutrino mode of ECEC as depicted in Figure 1.2 for the ^{130}Ba example. An experimental observation of

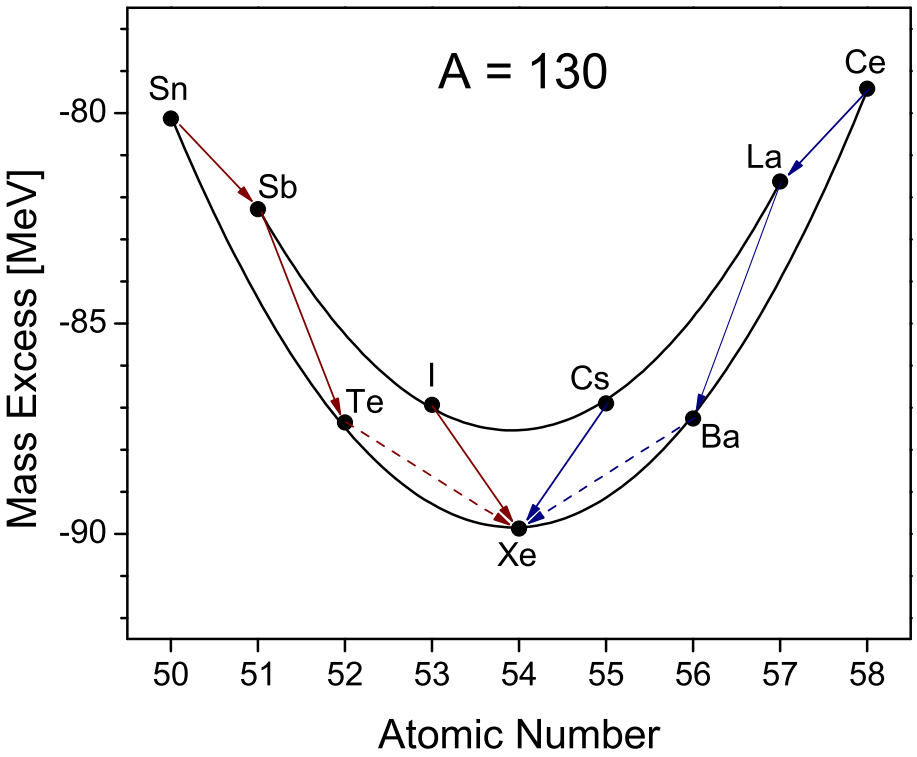

Figure 1.1: A = 130 odd-odd and even-even mass parabolas using 2012 AME mass excesses [7]. Although most nuclei can compensate for an excess of protons or an excess of neutrons through single-nucleon decay processes (solid arrows), such processes are energetically forbidden in ^{130}Ba and ^{130}Te because of nuclear pairing effects. These nuclei can only decay through feeble two-nucleon processes (dashed arrows) e.g. double electron capture in ^{130}Ba to ^{130}Xe.

0νECEC would prove the Majorana nature of neutrinos, and a measurement of the half-life could be used to determine the effective mass of the electron neutrino. In addition, an observation of 0νECEC would indicate lepton number nonconservation and thus physics beyond the current standard model, which entails the conservation of total lepton number [8].

Despite the potential scientific impact, the experimental feasibility of 0νECEC detection has long been regarded with justified skepticism. Indeed, the zero-neutrino mode is typically much weaker than the already feeble 2νECEC. Some hope for the observation of 0νECEC, however, is founded in a resonant enhancement of the process when either the ground or an

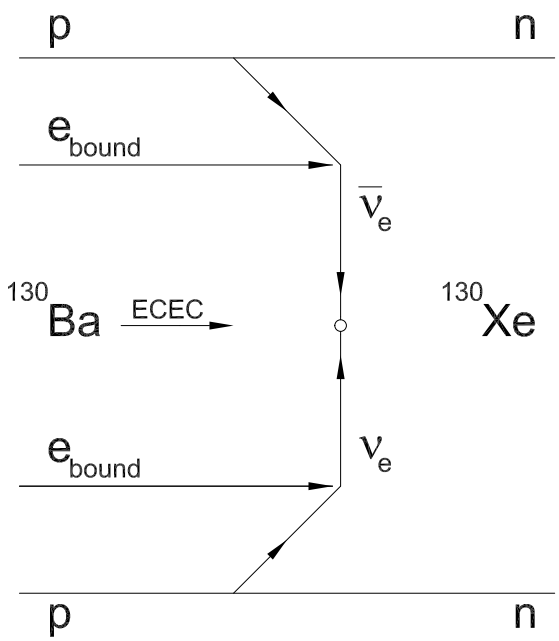

Figure 1.2: Feynman diagram illustrating the zero-neutrino mode of double electron capture for Majorana neutrinos.

excited state of the daughter is nearly degenerate with the parent. Resonant enhancement, first proposed by Winter in 1955 [9], has later been analyzed by Sujkowski and Wycech [10] who estimate that degeneracy could lead to a $\sim 10^6$ increase in the decay rate of a specific transition. In the case of good degeneracy and strong enhancement, the zero-neutrino mode could become much more dominant than competing 2νECEC process [11].

Resonance enhancement is based on minimizing the so-called degeneracy parameter, Δ, term of the 0νECEC decay rate, $\lambda_{\epsilon\epsilon}$,

$$\lambda_{\epsilon\epsilon} = \frac{\mathcal{M}^2}{\Delta^2 + \Gamma^2/4}\Gamma, \tag{1.3}$$

where Γ is the sum of the nuclear width and the two-electron-hole width, and $\mathcal{M}^2$ is the product of the leptonic phase-space factor, the nuclear matrix element squared, and the effective neutrino mass squared [12]. The degeneracy parameter is the Q value, energy

difference between mother and daughter atoms, less the binding energy of the two-electron hole, B_{2h}, and the excitation energy of the daughter, E_γ: $\Delta = Q_{\epsilon\epsilon}$ - B_{2h} - E_γ. In general, Δ is large and hampers the decay rate of 0νECEC; Δ is typically hundreds of keV whereas Γ is generally tens of eV or less. The hope of resonance enhancement is to find a suitable 0νECEC candidate where the energy of the decay is well balanced, i.e. where $Q_{\epsilon\epsilon}$ is equal to the sum of E_γ and B_{2h} to within a few tens of eV. In this case, Δ would be on the order of Γ, and the decay rate would be greatly enhanced. When considering possible captures to excited states, the conservation of spin must be taken into account. The parity should also be conserved so that the decay rate is not suppressed.

1.2.1.3 Overview of 0νECEC candidates and the need for an improved determination of the ^{78}Kr double-electron capture Q value

In the early eighties, Bernabeu, De Rujula, and Jarlskog studied the neutrinoless double electron capture candidates and identified, with the experimental data available at the time, the 12 candidates that appeared to have the most merit for resonant enhancement [11]. The merit, however, was ambiguous because of the large uncertainty of the double electron capture Q values for all 12 candidates. At the time, atomic mass measurement techniques were not yet sufficiently developed to reach the precision required to confirm resonance enhancement. Mass measurement techniques have improved greatly since then, and in the last five years Penning trap mass spectrometry has been used to determine $Q_{\epsilon\epsilon}$ for ten of the 12 original 0νECEC candidates with sufficient precision to confirm or exclude resonance enhancement [13, 14, 15, 16, 17, 18, 19, 20, 21, 22]; Table 1.1 lists the updated Q values for the 12 cases proposed by Bernabeu et al. Penning trap mass spectrometry has also been used to investigate additional 0νECEC candidates not included in this original list

Table 1.1: Double-electron capture Q values for the 12 original 0νECEC candidates identified by Bernabeu et al. [11]. For the ten cases where $Q_{\epsilon\epsilon}$ was determined via Penning trap mass spectrometry, the location of the measurement is listed. For the two cases that lacked a direct measurement, ^{78}Kr and ^{196}Hg, the listed Q value was computed using the atomic mass value of the mother and daughter given in the 2012 Atomic Mass Evaluation [7].

Transition	$Q_{\epsilon\epsilon}$ (keV)	$\sigma(Q_{\epsilon\epsilon})$ (keV)	Penning trap measurement
^{74}Se$\rightarrow$ ^{74}Ge	1209.169	0.049	JYFLTRAP, JYFL [13]
	1209.240	0.007	FSU-MIT Trap, FSU [14]
^{106}Cd$\rightarrow$ ^{106}Pd	2775.39	0.10	SHIPTRAP, GSI [15]
	2775.01	0.56	TRIGA-TRAP, MPIK [16]
^{164}Er$\rightarrow$ ^{164}Dy	25.07	0.12	SHIPTRAP, GSI [17]
^{112}Sn$\rightarrow$ ^{112}Cd	1919.82	0.16	JYFLTRAP, JYFL [18]
^{152}Gd$\rightarrow$ ^{152}Sm	55.70	0.18	SHIPTRAP, GSI [19]
^{168}Yb$\rightarrow$ ^{168}Er	1409.27	0.25	SHIPTRAP, GSI [20]
^{180}W$\rightarrow$ ^{180}Hf	143.20	0.27	SHIPTRAP, GSI [21]
^{130}Ba$\rightarrow$ ^{130}Xe	2623.74	0.29	SHIPTRAP, GSI [22]
^{162}Er$\rightarrow$ ^{162}Dy	1846.95	0.30	SHIPTRAP, GSI [20]
^{102}Pd$\rightarrow$ ^{102}Ru	1203.27	0.36	SHIPTRAP, GSI [15]
^{78}Kr$\rightarrow$ ^{78}Se	2846.31	0.72	
^{196}Hg$\rightarrow$ ^{196}Pt	820.1	3.1	

[15, 16, 20, 22, 23, 24, 25].

Despite the great progress in the determination of $Q_{\epsilon\epsilon}$ for many of the 0νECEC candidates, a direct measurement of $Q_{\epsilon\epsilon}$ was lacking for two of the original candidates, ^{78}Kr and ^{196}Hg. In order for 0νECEC to the candidate 688.693 (5) keV [26], 2^+ excited state of ^{196}Pt to be maximally enhanced, the actual Q value would have to be $\sim$41 keV less than $Q_{\epsilon\epsilon}$ from the 2012 Atomic Mass Evaluation [7] (listed in Table 5.1). Thus, even with the large uncertainty of $Q_{\epsilon\epsilon}$, the 2^+ excited state of ^{196}Pt can confidently be excluded from candidates that could lead to resonant enhancement. The potential for resonance enhancement of 0νECEC for ^{78}Kr is not as clear cut. Maximum enhancement of 0νECEC to the identified 2838.49 (7) keV [26], 2^+ excited state of ^{78}Se requires a shift of $\sim$5 keV from the value of $Q_{\epsilon\epsilon}$ listed in Table 1.1; this listed value is obtained using the 2012 AME atomic mass values

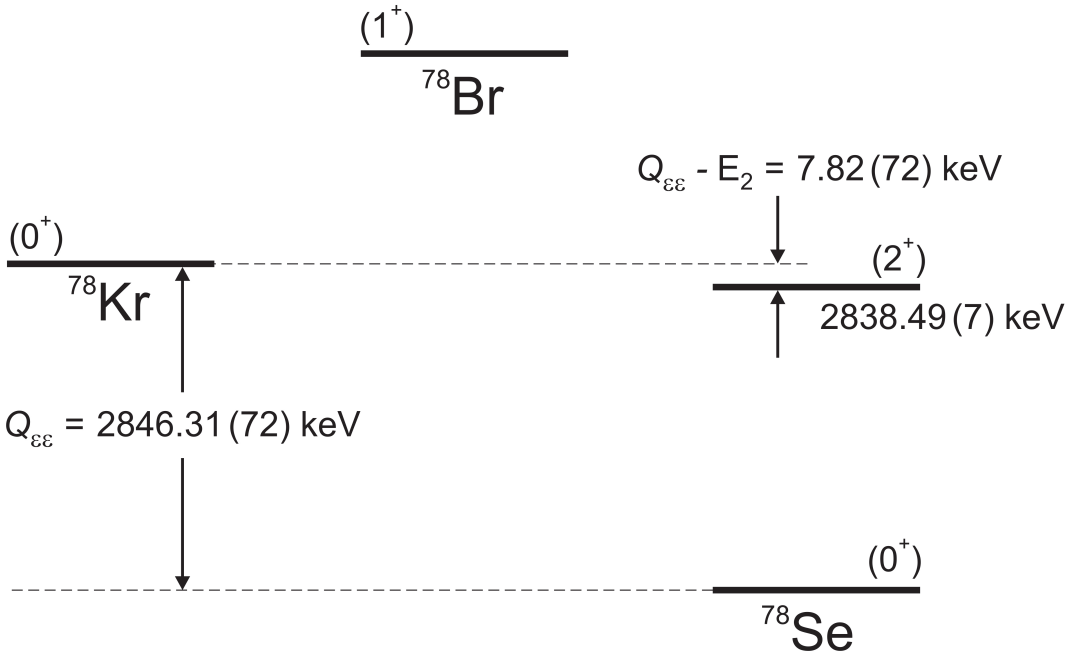

Figure 1.3: Scheme of the possible enhancement of neutrinoless double electron capture in ^{78}Kr to the (2^+) excited state of ^{78}Se.

of ^{78}Kr and ^{78}Se [7]. See Fig. 1.3. The 2012 AME atomic mass value of ^{78}Kr is based on Penning trap mass measurements, but the 2012 AME value of ^{78}Se is based exclusively on reactions. In particular, ^{77}Se(n,γ) is 99% of the influence of the 2012 AME atomic mass value of ^{78}Se. Two thirds of the influence of the ^{77}Se(n,γ) value [7, 27] is from the 2007 evaluation of neutron separation energies by the International Atomic Energy Agency [28], and one third of the value of ^{77}Se(n,γ) is based off the neutron separation energy derived from the 1981 thermal measurement at Brookhaven National Laboratory [29]. Given the indirect methods used to determine the ^{78}Kr double electron capture Q value, one cannot confidently exclude the possibility of resonance enhancement. Thus, a direct measurement of the ^{78}Kr double electron capture Q value would be beneficial in order to better evaluate the potential for resonance enhancement.

1.2.2 Double beta decay

1.2.2.1 Introduction

Figure 1.1 illustrates another example of a feeble two nucleon process besides the mentioned double electron capture in ^{130}Ba. In this example decay from ^{130}Te to ^{130}Xe, two neutrons are converted into two protons, and two electrons and two antineutrinos are emitted.

$$2n \longrightarrow 2p + 2e + 2\bar{\nu}_e \text{ (occurs in a nucleus)} \tag{1.4}$$

To observe this decay, known as two neutrino double beta ($2\nu\beta\beta$) decay, it is necessary to consider candidate nuclei where single beta decay is either forbidden or highly suppressed. There are 35 double beta decay candidates [5]; $2\nu\beta\beta$ decay has been detected and the half-life measured for many of them [30].

If neutrinos are their own antiparticles, i.e. are Majorana particles, then a zero neutrino mode of the process, known as neutrinoless double beta ($0\nu\beta\beta$) decay, is also possible. The detection of $0\nu\beta\beta$ decay would confirm the Majorana nature of neutrinos. If the corresponding phase space factor $G_{0\nu}$ and nuclear matrix element $M_{0\nu}$ are computed, then a measurement of the half-life $T^{0\nu}_{1/2}$ could be used to determine the effective mass of the electron neutrino $\langle m_{\beta\beta}\rangle$ via

$$(T^{0\nu}_{1/2})^{-1} = G_{0\nu}(Q_{\beta\beta}, Z)|M_{0\nu}|^2(\langle m_{\beta\beta}\rangle/m_e)^2, \tag{1.5}$$

where Z is the nuclear charge and m_e is the electron rest mass.

The experimental signature of $0\nu\beta\beta$ decay is a pair of electrons detected in coincidence with a combined total energy equal to $Q_{\beta\beta}$. Detection of $0\nu\beta\beta$ decay, however, is exper-

imentally challenging; the limits from $0\nu\beta\beta$ decay experiments indicate that the half-lives for neutrinoless double beta decay are at least a factor of $\sim 10^4$ longer than the half-lives of the two neutrino mode [30]. Therefore, accurate knowledge of the Q value of double beta decay candidates is important for resolving the $0\nu\beta\beta$ decay peak from the background of the more dominant two neutrino mode as well as from other typical sources of background. In addition, a reliable determination of $Q_{\beta\beta}$ is vital for extracting the effective neutrino mass from Eq. 1.5 if the half-life of a $0\nu\beta\beta$ process was determined by experiment. Extracting the effective neutrino mass from a measurement of the half-life is also theoretically challenging because it requires accurate knowledge of the relevant nuclear matrix element.

1.2.2.2 Overview of $0\nu\beta\beta$ decay candidates and summary of Penning trap measurements of double beta decay Q values

Candidate nuclei with a large Q value are ideal choices for double beta decay experiments since the phase space factors, and hence the decay rate, is enhanced as $G_{0\nu} \propto Q_{\beta\beta}^5$ and $G_{2\nu} \propto Q_{\beta\beta}^{11}$ for the zero and two neutrino modes, respectively. Thus of the 35 double beta decay candidates, the 11 with $Q_{\beta\beta} > 2$ MeV have the most potential. Recognizing the importance of high precision Q value measurements, Penning trap groups at a variety of different facilities have performed direct measurements of nine of these 11 double beta decay candidates (as of April 2013). The Q value measurements are listed in Table 1.2. ^{48}Ca and ^{96}Zr are the only two candidates with $Q_{\beta\beta} > 2$ MeV that were lacking a direct Penning trap measurement. A challenge of double beta decay experiments with these isotopes is the low natural abundance, which makes it difficult to procure a large amount of the isotopes for experiments. The natural abundances of ^{96}Zr and ^{48}Ca are 2.8% and 0.2% respectively.

Despite the low natural abundances, $2\nu\beta\beta$ decay in ^{48}Ca [38, 39, 40] and ^{96}Zr [40, 41] has

Table 1.2: Double beta decay Q values (status on April 2013) of the 11 candidate nuclei with $Q_{\beta\beta} > 2$ MeV. The 11 candidates are listed in order of greatest Q value. For the 9 candidates where $Q_{\beta\beta}$ was determined directly by Penning trap mass spectrometry, the trapping group and laboratory of the measurement are listed. For the two cases that lacked a direct measurement, ^{96}Zr and ^{48}Ca, the listed Q value is from 2012 Atomic Mass Evaluation [7].

Transition	$Q_{\beta\beta}$ (keV)	$\sigma(Q_{\beta\beta})$ (keV)	Penning Trap Measurement
^{48}Ca$\rightarrow$ ^{48}Ti	4266.96	0.39	
^{150}Nd$\rightarrow$ ^{150}Sm	3371.38	0.20	JYFLTRAP, JYFL [31]
^{96}Zr$\rightarrow$ ^{96}Mo	3349.02	1.98	
^{100}Mo$\rightarrow$ ^{100}Ru	3034.40	0.17	JYFLTRAP, JYFL [32]
^{82}Se$\rightarrow$ ^{82}Kr	2997.9	0.3	LEBIT, NSCL [33]
^{116}Cd$\rightarrow$ ^{116}Sn	2813.50	0.13	JYFLTRAP, JYFL [34]
^{130}Te$\rightarrow$ ^{130}Xe	2527.518	0.013	FSU-MIT Trap, FSU [35]
	2527.01	0.32	CPT, ANL [25]
	2526.97	0.23	JYFLTRAP, JYFL [34]
^{136}Xe$\rightarrow$ ^{136}Ba	2457.86	0.48	JYFLTRAP, JYFL [24]
^{124}Sn$\rightarrow$ ^{124}Te	2292.64	0.39	SHIPTRAP, GSI [22]
^{76}Ge$\rightarrow$ ^{76}Se	2039.006	0.050	SMILETRAP, MSL [36]
	2039.04	0.16	JYFLTRAP, JYFL [32]
	2039.061	0.007	FSU-MIT Trap, FSU [14]
^{110}Pd$\rightarrow$ ^{110}Cd	2017.85	0.64	ISOLTRAP, CERN [37]
	2017.8	1.2	TRIGA-TRAP, MPIK [16]

been detected directly in double beta decay experiments, and the half-life has been measured for both isotopes. A major advantage of both ^{48}Ca and ^{96}Zr is a large Q value; the pair have two of the top three greatest Q values of all candidates. In addition to boosting the decay rate, a large Q value helps ensure that the $0\nu\beta\beta$ peak is above typical sources of background, important in sensitive experiments with very low count rates. Both ^{48}Ca and ^{96}Zr have merit as $0\nu\beta\beta$ candidates, and a direct Penning trap measurement of $Q_{\beta\beta}$ for both candidates is desired.

1.2.2.3 Calcium-48 for neutrinoless double beta decay experiments

Calcium-48 has good potential for $0\nu\beta\beta$ decay experiments. ^{48}Ca has the greatest Q value of all candidates. Also, it is the only double beta decay candidate with a doubly closed nuclear shell and has the lowest mass number of all candidates. This nature of ^{48}Ca makes its nuclear matrix element the least difficult to compute of all double beta decay candidates. Very recently a calculation of the ^{48}Ca nuclear matrix element was published [42], which included effects of levels outside the valence space in a shell-model calculation. The work found a $\approx$75% increase in the nuclear matrix element compared to the result from a calculation restricted to the valence space alone. In addition to making sophisticated calculations of the nuclear matrix element more accessible, the relatively simple structure of ^{48}Ca may also make it amenable to new enrichment techniques that may be difficult for candidates with more complex atomic structures; see for example Ref. [43]. With continued improvement in enrichment techniques, ^{48}Ca will become an even more promising candidate for $0\nu\beta\beta$ decay experiments.

The CAlcium fluoride for the study of Neutrinos and Dark matters by Low Energy Spectrometer (CANDLES) III [44] $0\nu\beta\beta$ decay experiment that employs ^{48}Ca is already

under way. The detector system has been installed at the Kamioka underground laboratory beneath 2700 meters of water equivalent (MWE) shielding. The experiment features 96 CaF_2(pure) scintillators totaling 305 kg that are immersed in a liquid scintillator vessel surrounded by 62 large photomultiplier tubes. The whole detector apparatus is submerged in pure water which provides additional shielding from background. Key features of CANDLES III are the novel "two phase system" of the liquid scintillators [45] and the light-concentration system [46], which together will help obtain an energy resolution of better than 4% (FWHM) at $Q_{\beta\beta}$. The CANDLES series aims at realizing a sensitivity sufficient to detect $0\nu\beta\beta$ decay in ^{48}Ca at the $T^{0\nu}_{1/2} = 10^{26}$ year level.

The CAlcium Research for VEry Low neutrino mass (CARVEL) [47] $0\nu\beta\beta$ decay experiment has been proposed. The proposal calls for 50 modules, each containing an enriched $^{48}CaWO_4$ crystal, totaling $\approx$ 100 kg of enriched $^{48}CaWO_4$ and $\approx$ 16 kg of ^{48}Ca. At each end of the 50 modules is a high purity quartz-plastic scintillator light guide system and a photomultiplier tube (PMT). The shielding that will surround CARVEL consists of an internal active shield layer of plastic scintillator and external passive shield layers of copper, lead, and polyethylene. Preliminary tests for CARVEL have been performed at the Solotvina Underground Laboratory beneath 1000 MWE shielding. For these tests three (nonenriched) $CaWO_4$ crystals were used. Results from the test were used to estimate an energy resolution of 4% at $Q_{\beta\beta}$. Additional tests have been performed in which a $CaWO_4$ crystal was surrounded by liquid silicon oil. The increase in the light collection efficiency has led the group to estimate that an improved energy resolution of 2.5% is attainable with modest advances in the energy resolution of the $CaWO_4$ crystals. The anticipated sensitivity of CARVEL to the half-life of $0\nu\beta\beta$ decay in ^{48}Ca is $T^{0\nu}_{1/2} = 10^{27}$ year.

1.2.2.4 Motivation for an Improved Determination of the ^{48}Ca Double Beta Decay Q Value

The strong dependence of $0\nu\beta\beta$ decay on $Q_{\beta\beta}$ and the grand scale of ^{48}Ca $0\nu\beta\beta$ decay experiments is strong motivation for a high precision measurement of the Q value. There, however, had never been a direct measurement of the ^{48}Ca double beta decay Q value. In 2012, the LEBIT Penning trap mass spectrometer was used in a high precision measurement of the atomic mass of ^{48}Ca with $^{39}K^{+}$, $^{41}K^{+}$, and $^{40}Ca^{+}$ as reference masses [48]. The measured ^{48}Ca atomic mass differed from the 2003 AME [49] value by -10.64 keV but agreed with an unpublished preliminary update in AME 2011 [50]. The 2012 LEBIT measurement reduced the uncertainty of m(^{48}Ca) by a factor of 21 and 11 from the uncertainty of the 2003 and 2011 AME values respectively. In 2012, no such Penning trap measurement of m(^{48}Ti) was made. Therefore the previous AME value of m(^{48}Ti) had to be relied on to calculate $Q_{\beta\beta}$ for ^{48}Ca. A direct, mass doublet Penning trap determination of $\nu_c(^{48}Ca^{+})/\nu_c(^{48}Ti^{+})$ is highly preferred and is the ideal method to determine the ^{48}Ca double beta decay Q value.

1.3 Outline

In this document, an overview of the National Superconducting Cyclotron Laboratory and LEBIT is provided. The mass measurement techniques used at LEBIT are discussed. The development of the laser ablation ion source is described including design considerations and the process of realizing the source. Current LEBIT systematic effects are quantified with a cross reference measurement of carbon cluster ions produced via laser ablation. Results are presented from the first direct measurement of the ^{48}Ca double beta decay Q value, which used the tandem operation of the laser ablation and surface sources for ion produc-

tion. Finally, the first direct determination of the ^{78}Kr double electron capture Q value is presented, and the potential of ^{78}Kr as a candidate for neutrinoless double electron capture experiments is evaluated.

Chapter 2

The LEBIT Facility at NSCL

2.1 Radioactive Beam Production with the Coupled Cyclotron Facility

The Low Energy Beam and Ion Trap (LEBIT) facility is located at the National Superconducting Cyclotron Laboratory (NSCL) at Michigan State University. At NSCL high intensity rare isotope beams are produced by projectile fragmentation and in-flight separation. A diagram of the principal experimental equipment employed for production and mass filtering is shown in Fig. 2.1.

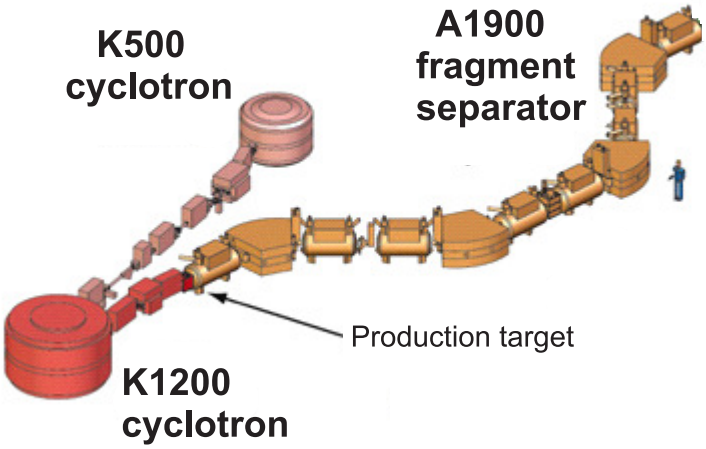

Figure 2.1: Diagram of the coupled cyclotron facility used for the production of pure rare isotope beams. A model of a person is included next to the fragment separator for a size reference.

After ionization with an Electron Cyclotron Resonance (ECR) ion source, the beam of heavy stable ions is injected into the K500 cyclotron. The ion beam is accelerated to ∼14 MeV/u and then sent to the K1200 cyclotron. The remaining electrons are then removed when passing through a stripper foil located near the center of the second cyclotron. The K1200 accelerates the beam to ∼140 MeV/u. The beam is then extracted and focused on a thick, light target for the production of rare isotopes. After the target, the secondary beam of reaction products retains most of the initial beam energy. The fragments are separated in flight with the A1900 [51], where in general isotopic separation is achieved by means of two dispersive beam-line sections separated by an energy degrading wedge.

The combination of projectile fragmentation and in-flight separation is a quick and chemistry independent method for the production of high intensity rare isotope beams. The NSCL, therefore, offers a great opportunity for experiments of many rare isotopes that are difficult to produce with different methods used at other rare isotope beam facilities.

2.2 Gas Catching Station

The rare isotope beams at NSCL can be used in a variety of high energy experiments. For the greatest precision in atomic mass measurements, however, the high-energy, high-emittance beam must be converted into a low-energy, low-emittance beam. After isotope filtering with the A1900 fragment separator, the secondary beam is sent to the gas catching station in order to accomplish the required conversion of beam properties for low energy experiments.

Prior to the gas catcher, the beam is slowed down by passing the beam through solid degraders. The ions then enter the gas catcher via a thin window. The gas catcher [52, 53] currently employed at NSCL was built by Argonne National Laboratory; see Fig. 2.2 . The

gas catcher is 1.2 meters long and is filled with helium gas at 120 mbar. The rare isotopes are thermalized through collisions with the helium buffer gas. Since helium has the highest first ionization energy of any ion, the rare isotopes remain at least singly charged after charge exchange reactions with the buffer gas. A static potential gradient is applied to drag the rare isotopes through the helium gas towards the opposite end of the gas catcher for extraction. In addition to the static potential gradient, an RF voltage is applied to adjacent cylindrical electrodes that line the chamber walls. The created RF-focusing "wall" [52] increases the efficiency of the device by reducing losses due to collisions with the chamber walls. Once the ions traverse the 1.2 meter cell, they are guided to the outlet nozzle by means of a coaxial conical "RF funnel". Extraction of the ions is aided by an additional push from the helium gas that is also passing through the extraction nozzle. After the nozzle, the ions pass through an ion guide system, built at NSCL, that features differential pumping and additional cooling. The low-energy, low-emittance continuous radioactive beam is

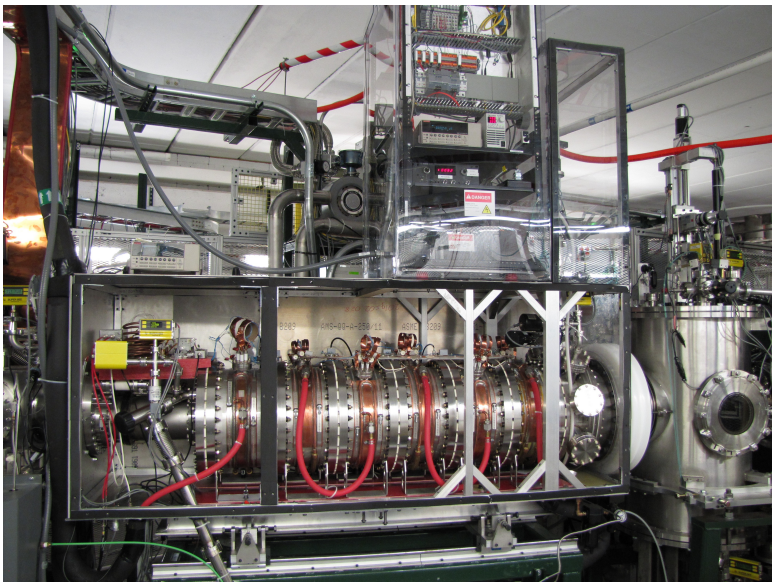

Figure 2.2: Linear gas catcher developed in collaboration with Argonne National Laboratory. The high energy rare isotope beam enters the catcher from the right side of the picture. The rare isotopes are thermalized in the gas catcher and extracted on the left side of the picture for transport to a variety of experimental groups.

accelerated to ∼60 keV for transport to a variety of different experimental groups including LEBIT for high precision Penning trap mass measurements.

2.3 Sources of Stable and Long-Lived Isotopes

In addition to radioactive beam from the gas catcher, LEBIT is connected to offline sources for ion production of stable and long lived isotopes. Prior to this work, a modified commercial ion source from Colutron Research Corporation had been the primary offline source utilized. The source is pictured in Fig. 2.3.

The source has been successful for ion production of alkali and alkali earth metals via surface ionization. Alkali vapor is created from impurities in the filament of the source when it is heated. To create vapor of an alkali earth metal, the metal can be loaded into a ceramic

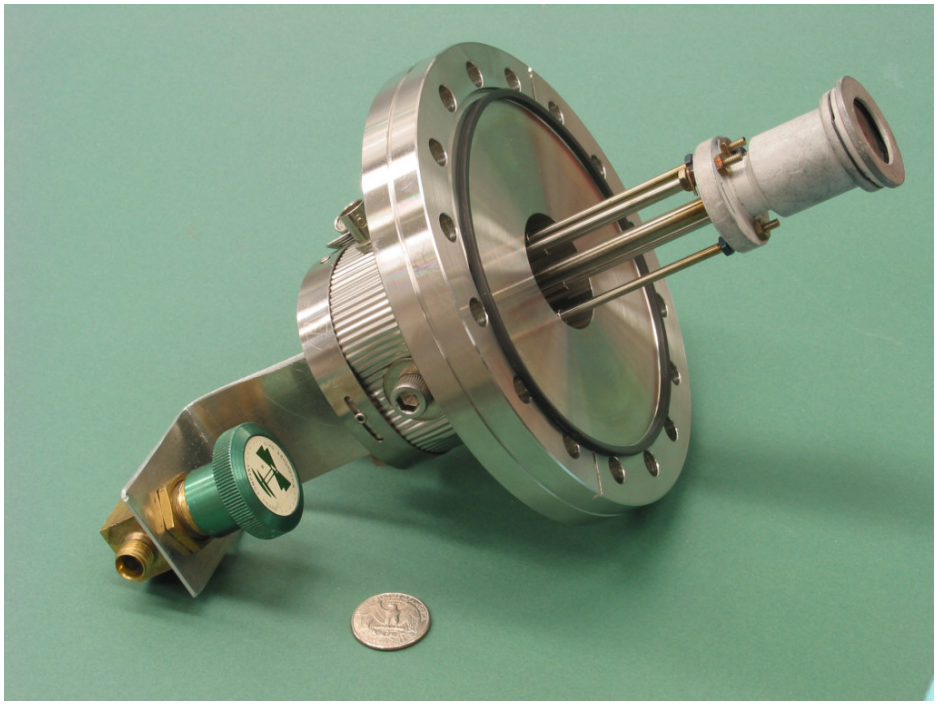

Figure 2.3: Ion source from Colutron Research Corporation that has been applied for ion production of alkali and alkali earth metals as well as for ion production of noble gases and elements with low melting points.

charge holder and inserted in the center of the heated filament coil. Once vaporized, the alkali or alkali earth gas is ionized by contact with the hot filament. The source is positively biased to ∼100V causing the ions to accelerate away from the filament. Although surface ionization has been successful for ion production of alkali and alkali earth metals, reliable production with this technique is limited to elements with an ionization potential of ∼ 7 eV or less [54, 55].

The source has also been operated successfully for ion production of noble gases. The desired noble gas is introduced into the chamber via a needle valve to a gas inlet tube. The filament is heated and negatively biased to ∼ -100V to emit electrons. At a suitable gas pressure ($\sim 10^{-6}$ mbar), a continuous discharge is formed ionizing the noble gas and generating a plasma. In addition, ion production of some elements with low melting points can be accomplished by operating the source in plasma mode. The desired element is loaded into a ceramic holder and vaporized as described above. A noble gas, such as helium, is similarly used as a support gas to produce a discharge, form a plasma, and ionize the vapor of the desired element. This technique has been successfully applied for ion production of elements with low melting points such as selenium. The method, however, cannot be extended to reliably produce ions of elements that are not easily amenable to vaporization techniques.

The continuous ion beam from the Colutron source is accelerated and transported downstream at 5 keV.

2.4 Beam Cooler and Buncher

The ion beam is decelerated to a few tens of eV by means of retardation electrodes and is then gathered into the beam cooler and buncher [56, 57] for the preparation of cooled ion bunches. The device is operated at LN_2-temperature and is divided into two separate regions for initial cooling and for beam bunching. For efficient cooling, the first section is filled with buffer gas (typically helium) at a pressure of $\sim 10^{-2}$ mbar. The ions are radially confined by a radio frequency quadrupole (RFQ) field created from four rod electrodes. The rods are surrounded by four wedge-type electrodes that are held at a static voltage. The field penetration from the wedge electrodes varies throughout the length of the cooler creating the axial electric field necessary to drag the ions through the buffer gas. As the ions travel through the cooler, the transverse emittance is reduced by collisions with the buffer gas.

After the cooler, the ions pass through a μRFQ which couples the initial cooling section and the bunching section. The μRFQ electrode structure is similar to that of the cooler but is much reduced in size. See Fig. 2.4. The μRFQ provides differential pumping enabling the buncher section to be held at a pressure 1-2 orders of magnitude lower than the initial

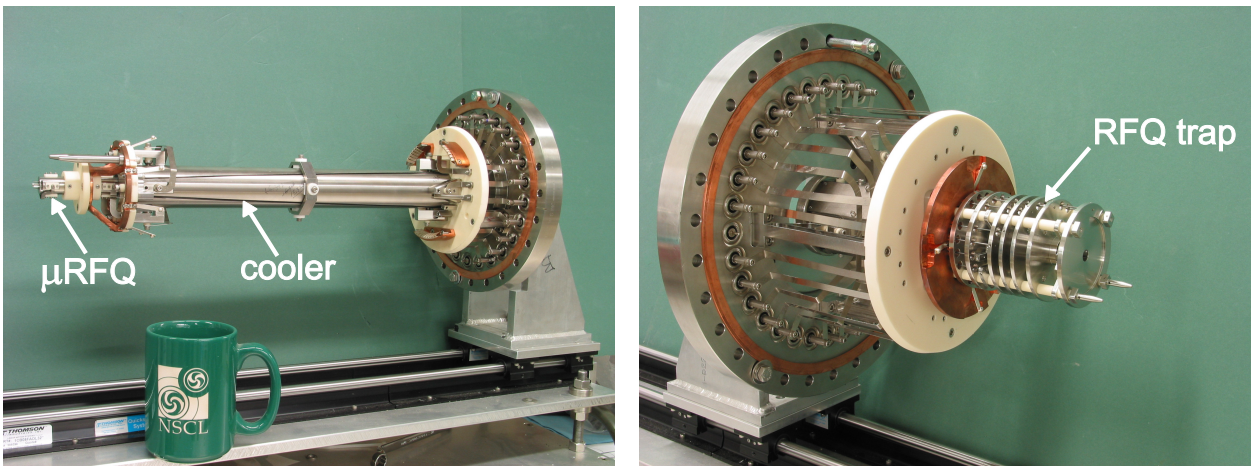

Figure 2.4: Cooler buncher electrodes removed from the vacuum chamber for easy viewing. A NSCL coffee mug is included in the picture as a size reference.

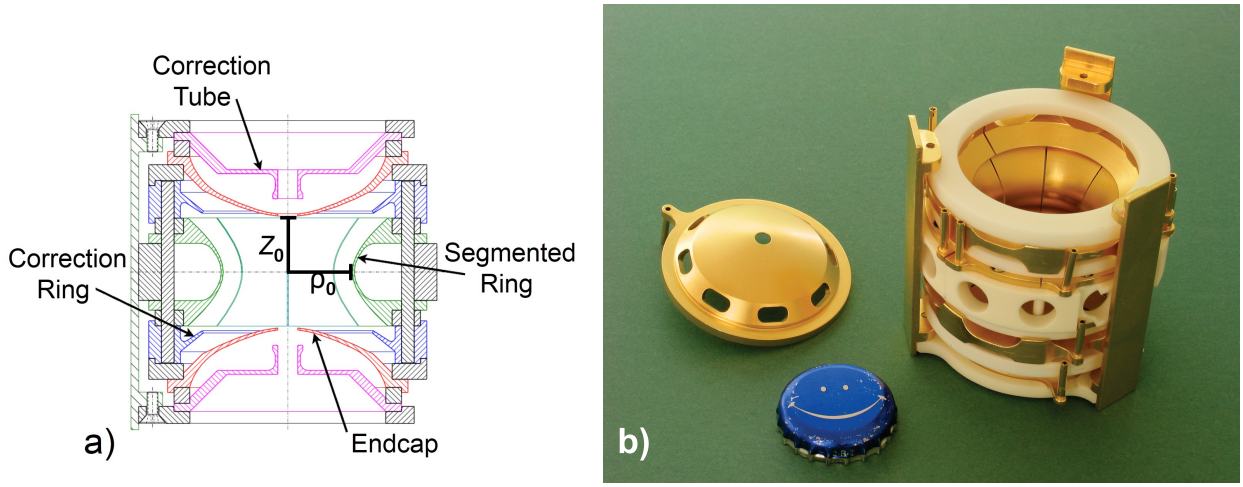

Figure 2.5: a) Design drawing of the LEBIT Penning trap. The electrodes (colored hatches) are labeled, and the standard trap dimension parameters, ρ_o and z_o, are shown. b) Photograph of the LEBIT Penning trap with one endcap removed.

cooling section. This lower pressure helps minimize reheating of the ions during extraction. In the bunching section, four RFQ rods are surrounded by seven cylindrical electrodes. A trapping potential for axial confinement can be created by applying suitable voltages to the cylindrical electrodes. The ions are typically held for ~30 ms for final beam cooling and are then extracted in low emittance, sub microsecond ion pulses.

2.5 Penning Trap Mass Spectrometer

2.5.1 Ion confinement with the LEBIT Penning trap

The cooled ion bunches are then transported to the Penning trap mass spectrometer [58, 59] for high precision measurements. The LEBIT Penning trap provides three dimensional confinement through a 9.4 T magnetic field (for radial confinement) and a static electric quadrupole potential (for axial confinement).

The quadrupole potential is generated from a potential difference U_o ~25 V between the

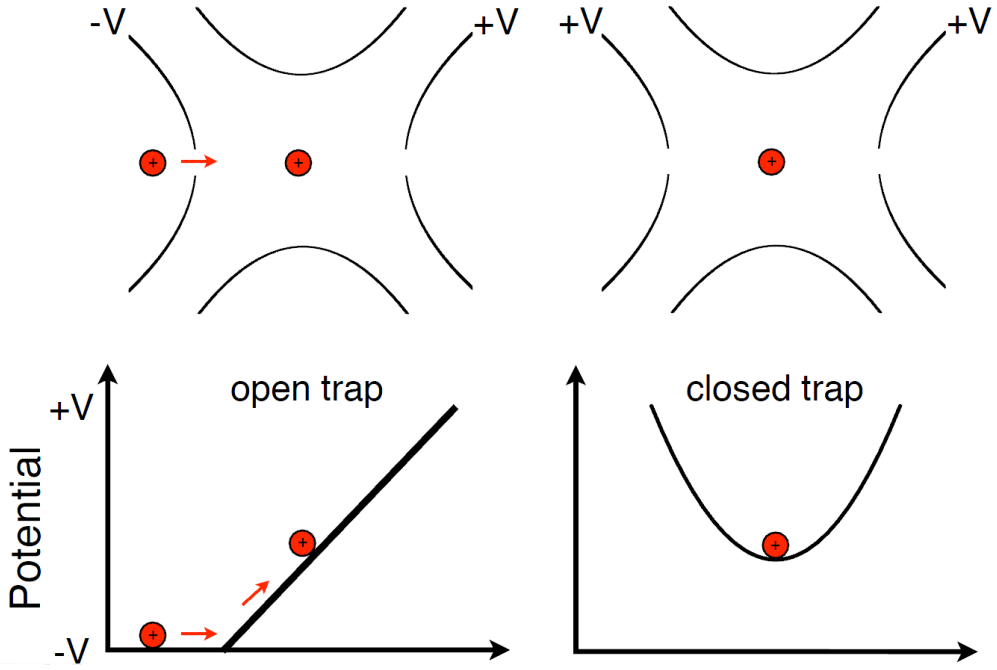

Figure 2.6: Cartoon illustrating the process of loading an ion into the Penning trap by the fast switching of the injection endcap potential.

hyperbolic endcaps and ring electrodes, shown in Fig. 2.5. The dimensions of the LEBIT Penning trap are characterized by the spacing of these electrodes. The inner radius of the ring electrode ρ_o is 13 mm, and the spacing between the endcaps $2z_o$ is 22.36 mm. These dimension parameters are depicted in Fig. 2.5. The parameter values were chosen to minimize deviations from a pure quadrupole potential [59]. In addition, the trap features correction ring and tube electrodes, which help compensate for the finite size of trap electrodes and the holes in the endcaps necessary for injection and extraction.

Ions are captured in the trap in a dynamic process. The potential of the injection encap is lowered allowing the ion bunch to enter the trap. Once the ion bunch enters the trap, the pontential of the injection cap is rapidly raised creating a parabolic trapping potential in the axial direction. Fig. 2.6 shows a cartoon of this process. Injection into the trap is optimized by adjusting the slope of the injection potential such that the ion bunch is at the trap center

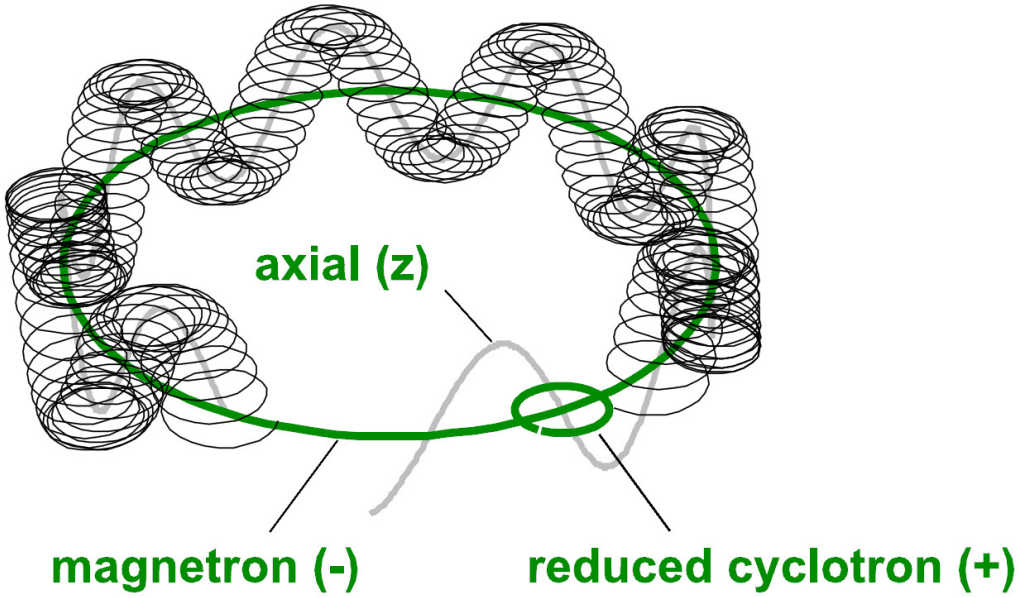

Figure 2.7: Motion of an ion in a Penning trap. In general, the motion is the superposition of three eigenmotions: axial, magnetron, and reduced cyclotron.

when the potential of the injection endcap is switched [59].

2.5.2 Ion motion in the Penning trap

Once captured in the trap an ion undergoes characteristic motion; the equations of which have been solved exactly for an ideal Penning trap [60]. In general the motion is the superposition of three independent eigenmotions: axial (z), magnetron (-), and reduced cyclotron (+). See Fig. 2.7. Each eigenmotion has an angular frequency ω_z, ω_-, and ω_+ respectively. These frequencies depend on the charge q and mass m of the ion as well as the magnetic field B, trap potential U_o, and the dimensions of the trap (ρ_o, z_o). The expression for the frequencies of the eigenmotions can be simplified by introducing the characteristic trap parameter $d = \sqrt{z_o^2/2 + \rho_o^2/4}$ and the true angular cyclotron frequency $\omega_c = \frac{qB}{m} = 2\pi\nu_c$ of the ion in only the presence of a magnetic field B. The frequencies of the eigenmotions in an

ideal Penning trap are then give by

$$\omega_z = \sqrt{\frac{qU_o}{md^2}}, \tag{2.1}$$

$$\omega_\pm = \frac{\omega_c}{2} \pm \sqrt{\frac{\omega_c^2}{4} - \frac{\omega_z^2}{2}}. \tag{2.2}$$

In general, $\omega_+ > \omega_z > \omega_-$. As an example for the LEBIT Penning trap parameters and a singly charged ion with mass number A = 50, ω_+, ω_z, and ω_- are roughly 20 MHz, 700 kHz, and 10 kHz respectively.

2.5.3 Traditional excitation methods of ion motion

The motion of an ion in a Penning trap can be manipulated by applying oscillating electric fields. Electric fields with various multipolarities and frequencies can be applied to drive the ion motion in order to achieve desired results. Applications of dipole and quadrupole excitations are described in this subsection.

2.5.3.1 Dipole excitation

In general, an oscillating dipole electric field can be applied at the frequency of any of the three eigenmotions of an ion. This results in an increased amplitude of the particular eigenmotion. Dipole excitation [4, 61] can be used as an effective method for driving contaminant ions out of the trap in order to prepare pure ion samples before a measurement. In particular at LEBIT, the strongly mass-dependent reduced cyclotron motion is the eigenmotion manipulated for purification purposes. An azimuthal dipole RF electric field is created by applying two RF signals (equal in amplitude and 180 degrees out of phase) to diametrically opposite

segments of the hyperbolic ring. The frequency of the dipole electric field is matched to the reduced cyclotron frequency of the contaminant ion to drive it out of the trap.

2.5.3.2 Quadrupole excitation

A quadrupole RF electric field can be applied with a frequency ω_{rf} equal to the sum or difference of two of the eigenfrequencies. This maximally couples the two eigenmotions and causes the ion motion to cycle back and forth from purely one eigenmotion to the other [4]. The most important application at LEBIT is the coupling of the two radial motions using a quadrupole excitation with a frequency $\omega_{rf} = \omega_+ + \omega_-$. The minimum period $2T_{conv}$ of the conversion between the two radial eigenmotions is given by

$$2T_{conv} = B\frac{a^2}{V_d}\frac{\omega_+ - \omega_-}{\omega_c}\pi, \tag{2.3}$$

where V_d is the amplitude of the excitation at radius a.

Reviewing the expressions for the frequencies of the radial eigenmotions in Eq. 2.2 shows a remarkable fact: for an ideal Penning trap, the frequency of the applied quadrupole RF electric field that maximally couples the two radial motions is exactly equal to the true cyclotron frequency of the ion, $\omega_c = \omega_+ + \omega_-$. Not only is this relation exactly true for an ideal Penning trap but it has also been shown by Brown and Gabrielse [62, 63] to hold remarkably well for a real Penning trap with realistic trap imperfections. The fact that a quadrupole excitation with $\omega_{rf} = \omega_c$ maximally couples the radial eigenmotions is the basis for cyclotron frequency determination at LEBIT.

2.5.4 Cyclotron frequency determination by the time of flight ion cyclotron resonance detection technique

The slow initial magnetron motion in the Penning trap [64] can be converted partially to reduced cyclotron motion by applying a quadrupole excitation with a frequency near the cyclotron frequency of the ion for a continuous period of T_{conv}. The conversion entails an increase in the radial kinetic energy, as $\omega_+ >> \omega_-$. The energy gain is maximum for full conversion of the two radial eigenmotions and is only possible in T_{conv} with maximum coupling, $\omega_{rf} = \omega_c$.

The maximum energy gain is thus a signal that the frequency of the applied quadrupole excitation is equal to the true cyclotron frequency of the ion. This fact can be used to precisely determine the cyclotron frequency of an ion. The time of flight ion cyclotron resonance technique [65] is the method currently used at LEBIT to determine when maximum energy gain has been achieved. After the quadrupole excitation, the potential of the ejection endcap is lowered to release the ion from the trap, and the time of flight (TOF) to a down stream microchannel plate (MCP) detector is measured. As the ion follows the magnetic field lines downstream towards the detector, it is accelerated by an axial force F in the inhomogeneous region of the magnetic field.

$$F = -\mu \frac{\partial B}{\partial z}, \tag{2.4}$$

where $\frac{\partial B}{\partial z}$ is the gradient of the magnetic field and μ is the magnetic moment of the orbiting ion. The magnetic moment is proportional to the radial energy of the ion [4]. Therefore, the increase in energy gained from the conversion of magnetron to reduced cyclotron motion

results in a reduced time of flight to the MCP. The minimum in time of flight corresponds to the maximum gain in radial energy by the full conversion to reduced cyclotron motion with $\omega_{rf} = \omega_c$.

The true cyclotron frequency of an ion can thus be determined by a series of time of flight measurements. A quadrupole excitation is applied with a frequency near the cyclotron frequency of the ion. The ions are released from the trap, and the TOF is measured. The frequency of the applied excitation is incremented, and the process is repeated for a new ion bunch. A cyclotron resonance curve, like the one in Fig. 2.8 a), is built up. Each data point represents the mean time of flight of ions for a given excitation frequency. The data are fitted with a theoretical line shape [66], and the true cyclotron frequency of the ion is determined by the excitation frequency that yields a minimum in time of flight.

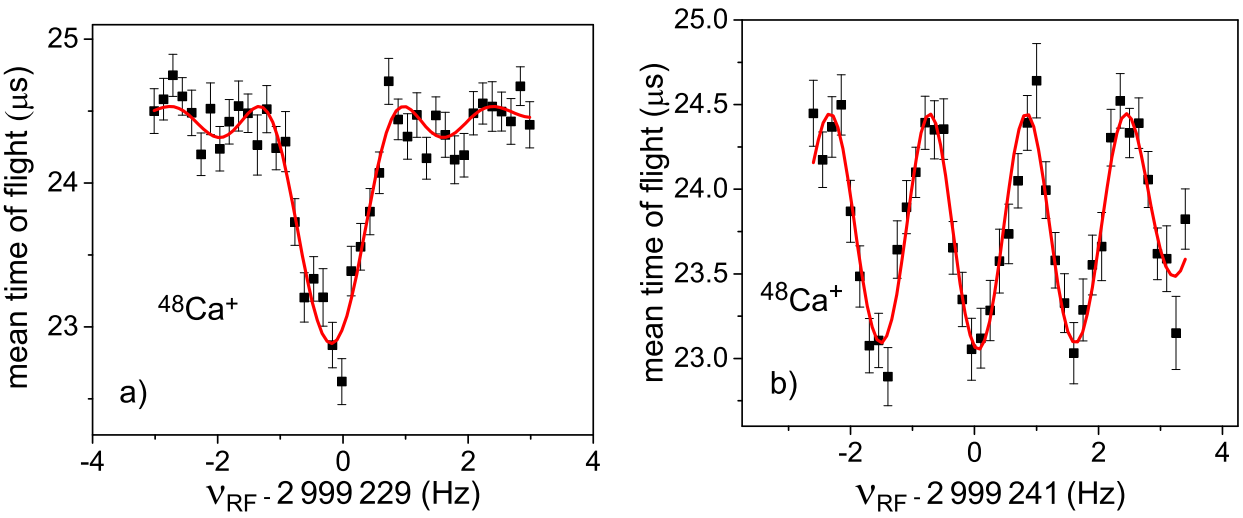

Figure 2.8: Time of flight ion cyclotron resonance curves using a traditional quadrupole excitation a) and Ramsey excitation method b). Each resonance was formed used a total excitation time of 750 ms, and approximately 1400 ions were detected for each resonance.

2.5.5 Ramsey Excitation Method

The technique of using separated oscillatory fields, originally invented by N.F. Ramsey for molecular beam experiments, has been applied to quadrupole excitation of stored ions in a Penning trap [67]. In the Ramsey excitation scheme, multiple (time separated) RF excitations are applied. This differs from the traditional method where a quadrupole excitation is applied for a continuous period. Ramsey fringes in the resonance curve are produced by allowing the phase of the ion to evolve between excitations and fixing the phase of each RF excitation with respect to the first. Many different line shapes can be produced by using different combinations of RF pulse numbers and wait time durations [68, 69]. The minimum full width half max of the central fringe, however, is obtained using two RF pulses. The two RF pulse excitation scheme, therefore, is ideal for precise determination of the cyclotron frequency. Fig. 2.8 b) shows a resonance curve using two 150 ms bursts of RF separated by a 450 ms period where no excitation is applied. The narrower, steeper, and more prominent nature of the fringes enables a more precise determination of the cyclotron frequency for a given total excitation time and number of ions. Thus, the Ramsey excitation method has been broadly employed and is becoming the dominant excitation method at many Penning trap facilities.

2.5.6 Mass determination via cyclotron frequency ratios

The mass m_{int} of an ion of interest can be determined by comparison of its measured cyclotron frequency with that of a reference ion with well known mass m_{ref}. Since the magnetic field strength is not exactly constant in time, it is important that the time of each reference measurement be as close as possible to the time of the ion of interest measurement. Taking

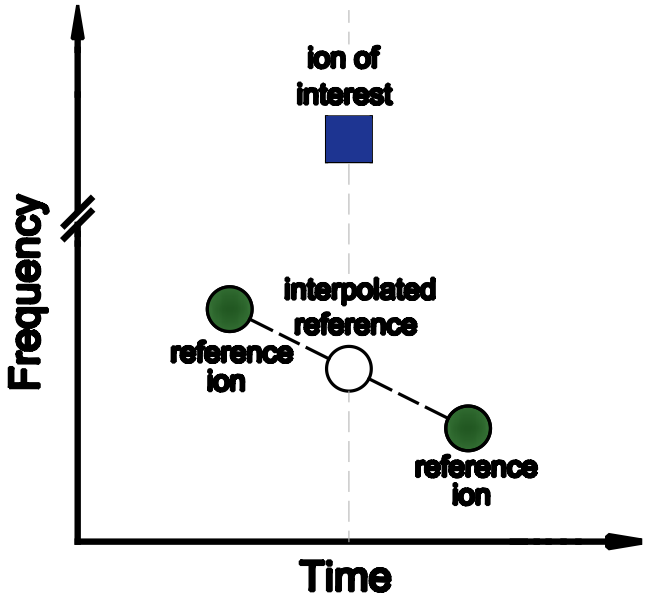

Figure 2.9: Illustration of the linear interpolation of reference measurements in order to determine the cyclotron frequency of the reference ion at the time of the ion of interest measurement. The mass of the ion of interest can then be determined through the cyclotron frequency ratio, provided the reference mass is known.

a reference resonance both before and after each ion of interest measurement is the general method for compensating for changes in the magnetic field strength. The bracketing pairs of reference resonances are then linearly interpolated to determine the cyclotron frequency of the reference ion $\nu_{c,ref}$ at the measurement time of the ion of interest; see Fig. 2.9. The mass of the ion of interest can then be determined by the cyclotron frequency ratio of the two ions: $m_{int} = (\nu_{c,ref}/\nu_{c,int})m_{ref}$. The mass of the electron is then added to determine the atomic mass of the isotope of interest. Typically the electron binding energy is negligible, but it can be corrected for if necessary in a very high precision measurement.

Chapter 3

Development of a Laser Ablation Ion Source for LEBIT

3.1 Laser ablation introduction

From its origin in 1962 [70], laser ablation has had a wide variety of applications ranging from nanosurgery to the fabrication of nanomaterials [71]. In order to modify the target material on the mesoscopic level and remove at least one tenth of target material monolayer per pulse, the technical definition of laser ablation, a power density of $\sim 10^8$ W/cm^2 [54] or more is required. As an example, for a laser pulse energy of $\sim$1 mJ and a pulse duration of $\sim$ 1 ns, a focus on the target with a beam spot diameter of $\sim$ 1 mm is required. With this power density, the interaction of the high-energy photons and the target material can cause the creation of a plasma. For details on the plasma plume refer to Ref. [71]. Various combinations of laser light and target properties can lead to many different types of interactions (e.g. electric sputtering, normal vaporization, normal boiling, and explosive boiling [72]). Laser ablation is not element specific and is thus an effective method for producing ions of many elements that span the periodic table. In this work laser ablation is applied for offline ion production at the LEBIT facility.

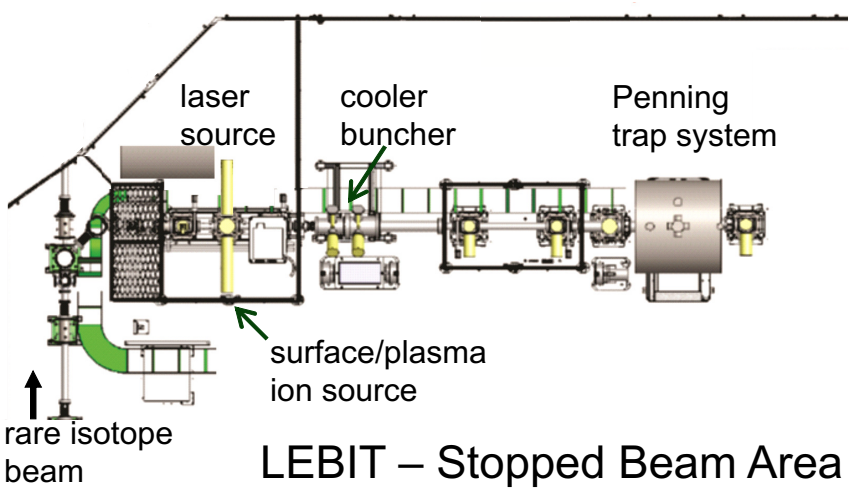

Figure 3.1: The LEBIT portion of the stopped beam area at NSCL. The position of the laser ablation source relative to the existing offline ion production methods is highlighted.

3.2 Concept and primary design considerations

Ions are produced with LAS by bombarding a target with 532 nm pulsed laser light from a neodymium-doped yttrium aluminum garnet (Nd:YAG) laser. Primary design considerations of LAS are discussed in this section including the location of the source, laser optics, target rotation, and ion optics.

3.2.1 Placement of the laser ablation source

An important consideration of designing the laser ablation source is how to best couple the new source with the existing experimental facility. It was decided that the ideal placement of LAS is directly opposite the surface and plasma ion sources and perpendicular to the main LEBIT beamline. In this configuration the existing electrostatic quadrupole deflector can be used to bend the ions produced with LAS 90 degrees and onto the axis of the LEBIT beamline. The position of the new ion source is depicted in Fig. 3.1.

3.2.2 Angle of incidence

One of the first design aspects of the laser source considered is the angle of incidence of the laser relative to the ablation target. Some successful laser ion sources, see Ref.[73] for example, were constructed such that the incoming laser light is perpendicular to the target. Having a nonzero angle of incidence, however, can facilitate laser entry, decrease the laser beam spot size on the target, and minimize back reflected light to the laser [54]. One facet of this possible configuration, though, that required investigation is whether an increased angle of incidence would significantly decrease the laser power transmitted to the target. Fresnel equations were used to estimate the extent of this effect; see for example Ref. [74]. The ratio of the power transmitted to the target to the total incoming power, i.e. the transmittance, was calculated as a function of incident angle for several different possible targets: titanium, carbon, molybdenum. The targets have a range of refractive indices: 1.84, 2.33, and 3.73 respectively [75]. As in Ref. [71], the refractive index of amorphous carbon was used to approximate that of Sigradur G. The resulting transmittances are shown as a function of incident angle in Fig. 3.2. For light with the electric field component perpendicular to the

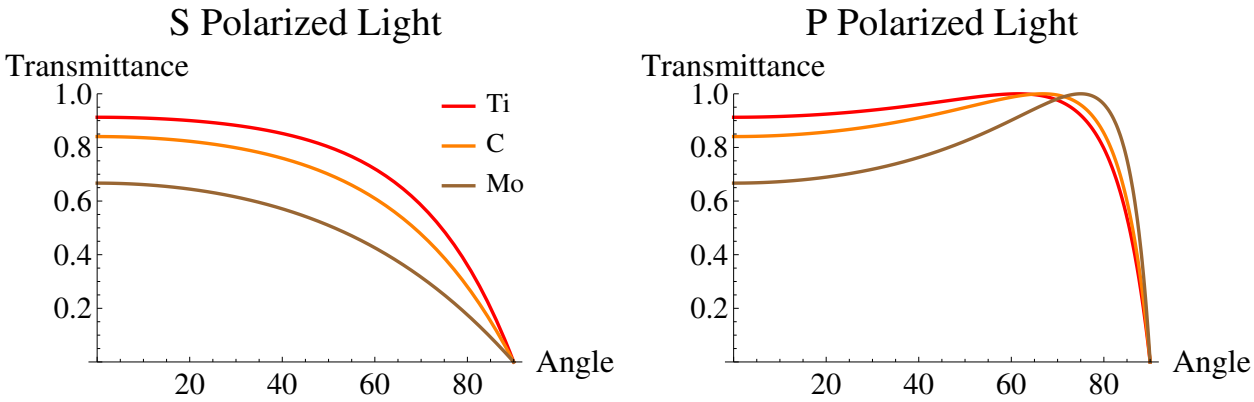

Figure 3.2: Transmittance calculated using Fresnel equations plotted as a function of incident angle. The results for titanium, carbon, and molybdenum targets are shown using refractive indices from Ref. [75] for 532nm, S and P polarized light.

plane of incidence, so called S polarized light, the transmittance falls off with increasing angle of incidence. For light with the electric field component parallel to the plane of incidence, P polarized light, the transmittance remains large for a wide range of incident angles. Based on this calculation, it was decided to ablate the target using P polarized laser light with a small angle of incidence.

3.2.3 Laser optics

A schematic of the laser ablation source design is presented in Fig. 3.3. The laser and all out-of-vacuum optics are housed adjacent to the vacuum chamber containing the ablation target and ion optics. The first laser optical element is a half-wave plate that converts the laser light from S to P polarization for the preferred transmittance properties. The laser light is reflected 90 degrees twice by a pair of mirrors; this setup helps fit all laser optics in a relatively small space. The mirrors are particularly useful for laser alignment and can be adjusted to achieve a laser beam spot at the desired position on the target. A beam splitter is located between the two mirrors and reflects 80% of the laser energy to a power/energy meter, which can be used to continuously monitor the laser power/energy. The maximum laser energy of 160mJ/pulse is substantially more than the pulse energy required for ion production. The beamsplitter, therefore, is helpful for reducing the laser energy to an energy that is closer to optimum for laser ablation. Fine tuning of the laser energy is

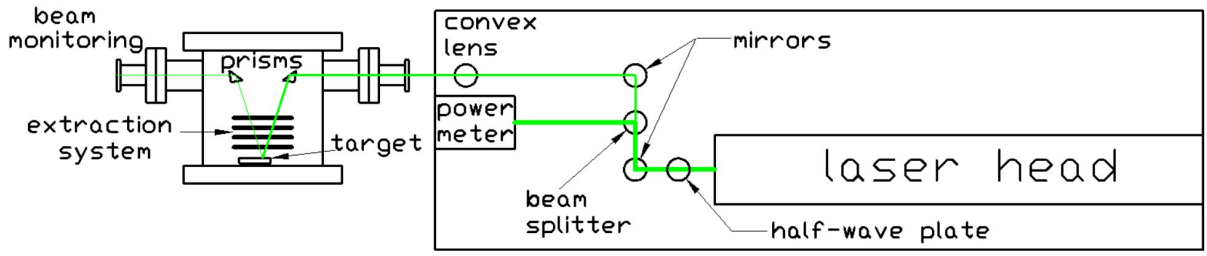

Figure 3.3: Schematic of the source design and the laser optical elements used for ablation.

done by varying the laser offset, a parameter of the laser that determines the energy of the emitted laser pulse. The only laser focusing element currently in use is a convex lens with a focal length f of 335 mm (for 532 nm wavelength light). It is important to have the convex lens close to the target since the laser beam diameter at the target increases with increasing focal length [76]. After this lens the laser enters the vacuum chamber parallel to the target via an optical window. An in vacuum right angle prism is used to reflect the laser light to the target and is tilted such that the laser has an 18 degree angle of incidence. An identical prism is similarly mounted on the opposite side of the vacuum chamber and can be used to view the laser beam spot on the target.

3.2.4 Optical telescope

Although not necessary for ion production, provisions have been made for an optical telescope which could be included in the future to further reduce the laser beam spot size on the target; see Fig. 3.4. This possible addition consists of including two more focusing elements prior to the convex lens currently employed. A plano concave lens could be added to increase the laser beam diameter at the existing convex lens. This would decrease the laser beam spot size at the target since the final laser beam diameter at the focus is inversely proportional to the laser beam diameter at the $f = 335$ mm convex lens [76]. Also, an additional convex lens could be added after the plano concave lens. Once the laser beam is spread out with the plano concave lens, the additional convex lens could be used to bring the light rays parallel. This has the practical advantage that the laser optics are essentially independent of the distance between the final convex lens and all other laser optics.

The decrease in the laser beam spot size with the implementation of an optical telescope can be estimated using ray matrices. For a plano concave lens with a focal length f_{cc}, radius

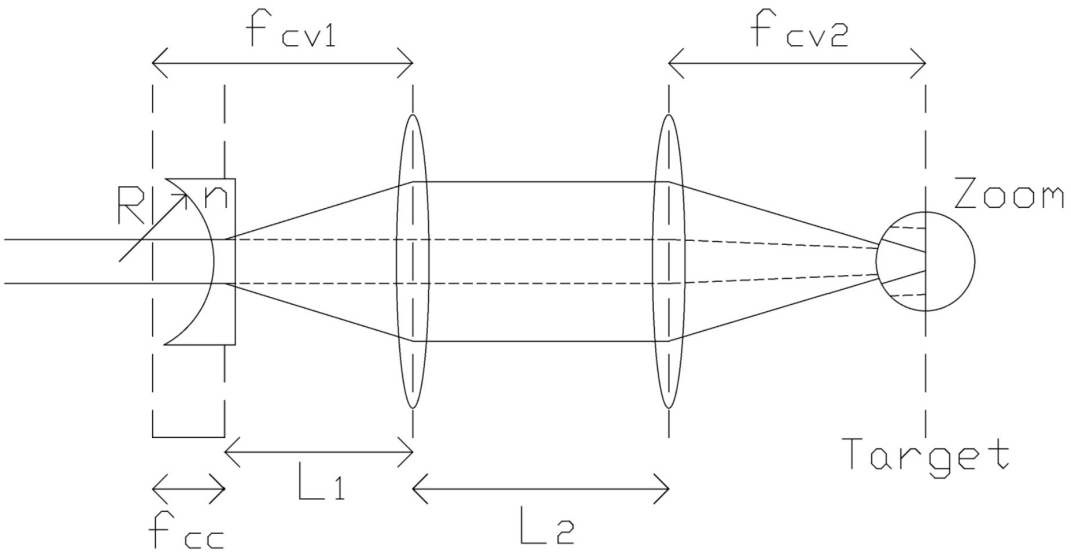

Figure 3.4: Depiction of how the addition of an optical telescope would lead to a decreased beam spot size at the target. The laser beam with the optical telescope (solid lines) is compared with that without the telescope (dashed lines.) Above the focal length of the plano concave lens is denoted as f_{cc}, and the focal lengths of the following two convex lenses are similarly labeled f_{cv1}, f_{cv2}. The length L_1 between the plano concave lens and the first convex lens is chosen to make the focus at the target practically independent of the length L_2 between the two convex lenses.

of curvature R, and an index of refraction n as well as a convex lens with a focal length of f_{cv1}, the diameter w and the divergence ϵ at the last convex lens can be expressed in terms of the initial beam diameter w_0 and divergence ϵ_0:

$$\begin{pmatrix} w \\ \epsilon \end{pmatrix} = \begin{pmatrix} 1 & L_2 \\ 0 & 1 \end{pmatrix} \begin{pmatrix} 1 & 0 \\ -1/f_{cv1} & 1 \end{pmatrix} \begin{pmatrix} 1 & L_1 \\ 0 & 1 \end{pmatrix} \begin{pmatrix} 1 & 0 \\ \frac{n-1}{R} & 1 \end{pmatrix} \begin{pmatrix} w_0 \\ \epsilon_0 \end{pmatrix}, \tag{3.1}$$

Equation 3.1 can be simplified by taking $\epsilon_0 = 0$, which is a very good approximation. L_1 and L_2 are the distance from the plano concave lens to the first convex lens and the distance between the two convex lenses respectively. L_1 is chosen such that after the beam diameter is increased with the plano concave lens, the first convex lens bends the light rays so that the focus is at infinity i.e. $L_1 = f_{cv1}$ - $|f_{cc}|$ [76]. Therefore, w is only very weakly dependent

on L_2. For a plano concave lens with focal length f_{cc} = -24.8 mm and a convex lens with focal length f_{cv1} = 99.1 mm, then L_1 = 74.3 mm , and L_2 can be taken as $\sim$ 50 mm. Then for a plano concave lens with R = 12.9 mm and n = 1.52, $w = 4w_0$. This factor of 4 increase in beam diameter at the last convex lens ultimately leads to a factor of four decrease in the laser beam spot size at the target [76].

3.2.5 Target rotation

The ablation process partially destroys the target. One option to minimize laser drilling effects and maximize target lifetime is to continuously move the laser beam, so it strikes many different parts of the target. While this method is effective at utilizing a large portion of the target, one disadvantage is that ion production occurs at many different locations with respect to the ion optics for extraction and focusing. An alternative approach is to keep the laser beam fixed and move the target. A particularly simple method is to offset the geometrical center of the circular target from the axis of the beam line and spin the target. While the target rotation method does not utilize as much of the target as other more sophisticated methods like the Lissajous raster scan system [71], the ion production point with respect to the ion optics is always the same with this method. After contemplation, it was decided to design the LEBIT laser ablation ions source with the target rotation method.

In order to provide the 5 kV potential difference necessary to accelerate the ions to 5 keV, the target is mounted after a high voltage (HV) break. Thus the LEBIT beamline prior to the cooler buncher can operate on the normal -5 keV bias, while the target rotation system can remain at true ground during normal offline operation. To provide the required target rotational offset, the two ends of the HV break are offset by 5 mm. In addition, a second 5 mm offset is incorporated into the reducer flange from which the target rotary feedthrough is

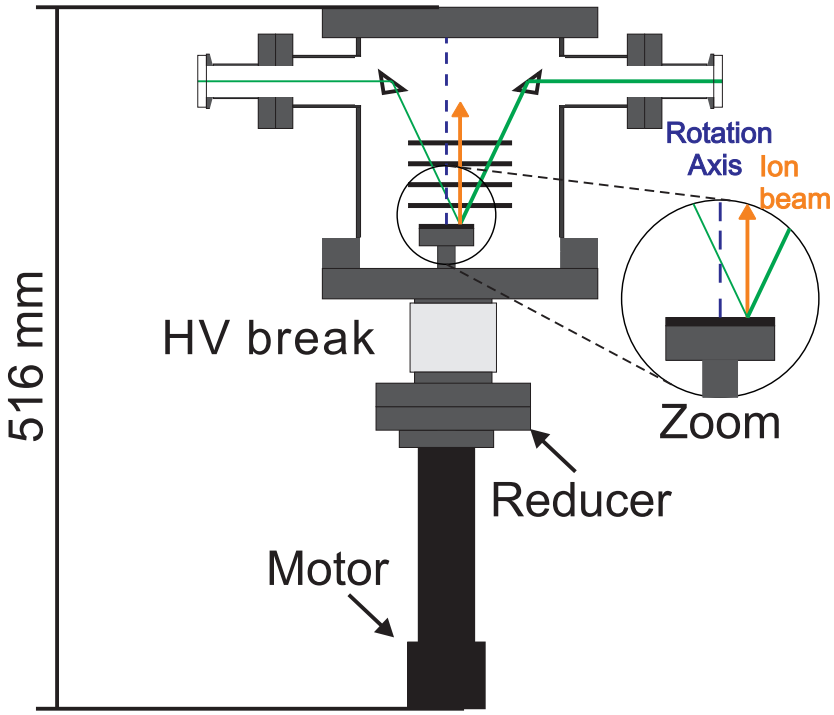

Figure 3.5: Illustration of LAS highlighting the rotational offset between the laser beam spot and the axis of rotation. The two 5 mm offsets incorporated into the HV break and reducer are here coupled to produce a 10 mm offset for rotation purposes.

mounted. During normal operation these two offsets add. The laser beam strikes the target 10 mm from the geometrical center of the circular target; see Fig. 3.5. When the target is rotated a circular track with a 20 mm diameter is etched by the laser. To help ensure parallel extraction of the ions, standard LEBIT LAS targets are large, 40 mm in diameter. The design of the LEBIT LAS, however, allows for the possibility of much smaller targets, which could be necessary if the target material is expensive or radioactive. For much smaller targets when rotation may not be practical, the source can be adjusted so that the two 5 mm offsets are 180 degrees out of phase and cancel so that the laser hits the target at its geometric center.

3.2.6 Ion transport after ablation

An essential criterion of the laser source design is that the LAS ion optics could be used in conjunction with the existing LEBIT optical elements to focus the beam such that it would be accepted into the ion cooler and buncher [56]. The necessary condition to achieve this for a 5 keV ion beam is an emittance less than 2.75 mm x 15.1π mrad = 41.5 π mm mrad at the entrance of the buncher.

The ion optics simulation program SIMION was used to investigate what LAS optical elements would be required in addition to the existing two electrostatic Einzel lenses after the 90 degree bender. See Fig. 3.6 for an overview of the elements of the simulation. A four ring system was modeled for extraction and acceleration to 5 keV beam energy. Each ring has an inner diameter and outer diameter of 30 mm and 76 mm respectively. An electrostatic quadrupole triplet was modeled for additional focusing prior to the 90 degree bender. The triplet consists of three 100 mm sections each with an internal diameter of

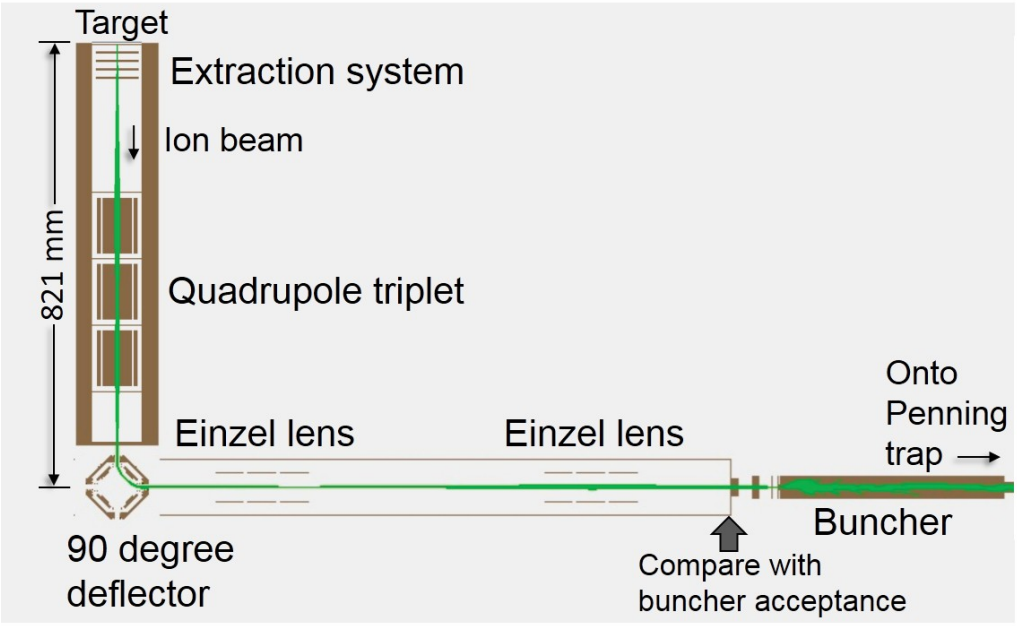

Figure 3.6: Simulation model used to determine the ion optics required for extraction and focusing after ablation in order to ensure successful acceptance into the ion cooler and buncher.

Table 3.1: Optimum voltages of the extraction system and electrostatic quadrupole triplet for a 5 keV beam determined by simulation. Below the rings are numbered with ring 1 being closest to the target. The two outer sections of the triplet have the same potential and provide horizontal focusing, while the inner third of the triple provides vertical focusing.

Extraction System	
Electrode	Voltage/ V
Ring 1	-1 250
Ring 2	-2 500
Ring 3	-3 750
Ring 4	-5 000

Quadrupole Triplet	
Section	Voltage/ V
Inner	$\pm$ 550
Outter	$\mp$ 375

55 mm. To accelerate the beam after ablation, simulations indicate (not surprisingly) that it is best to augment the voltages on the four rings of the extraction system in even intervals. Since the 90 degree bender introduces more distortion in the horizontal direction [57], it is advantageous to use the two outer sections of the triplet to focus horizontally. To achieve a similar vertical focus with the middle section of the triplet, greater voltages have to be applied. Table 3.1 lists the optimum settings found with SIMION for a 5 keV beam. With these optimum settings, simulations were used to check the emittance of the beam directly

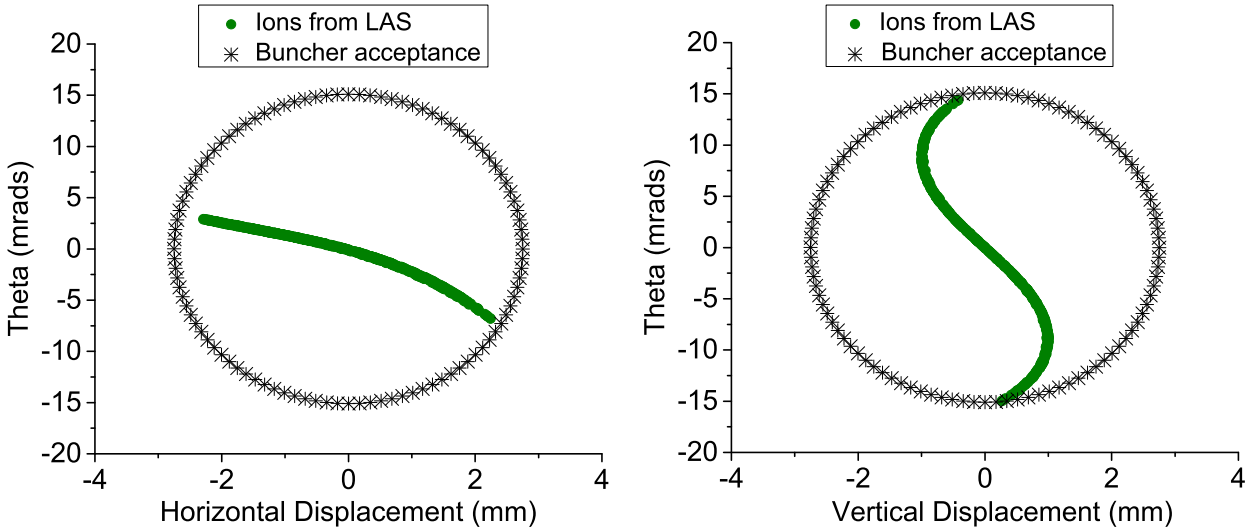

Figure 3.7: Simulation comparing the beam properties of LAS produced ions (green circles) directly before the cooler and buncher with the buncher acceptance (depicted with black asterisks). Results indicate that ions produced with LAS are accepted into the cooler and buncher without losses.

prior to the buncher. The emittance was found sufficient for acceptance into the buncher without losses. The beam properties compared to those required for buncher acceptance are shown in Fig. 3.7. Once the ions are successfully accepted into the buncher, previously established methods can be used to transport the ions to the Penning trap for measurements.

3.3 Realization of LAS

3.3.1 Laser Optics

The laser for the source is a Quantel Brilliant laser and has been repurposed from the previous NSCL laser source, which was used to characterize the gas cell in 2006 [71]. The Brilliant laser is a pulsed Nd:YAG laser with a second harmonic module for outputting 532 nm laser light. The laser features a maximum energy per pulse of 160 mJ, an initial beam diameter of 4.5 mm, a pulse duration of 4 ns, and a repetition rate of 20 Hz.

In addition to repurposing the laser, the power meter and some of the laser optics (half-wave plate and mirrors) necessary for LAS have also been repurposed from the previous laser source. For the prisms and lenses, the optical elements with the desired dimensions and focal lengths were procured from CVI Melles Griot and Edmund Optics. All optical elements have high damage thresholds, $\sim$3 J/cm^2 or higher for the above laser properties. Also, the f = 335 mm convex lens was chosen with a large beam diameter, 50.8 mm, to accommodate the possible future implementation of an optical telescope.

The laser head and all laser optics out of vacuum are secured on a Newport optical table; see Fig. 3.8. Vibrations are minimized by setting the optical table on four elastomeric vibrational isolators. The optical table is enclosed in a stand constructed with 80/20 Inc. aluminum frames and black anodized aluminum panels to minimize reflection. The enclosure

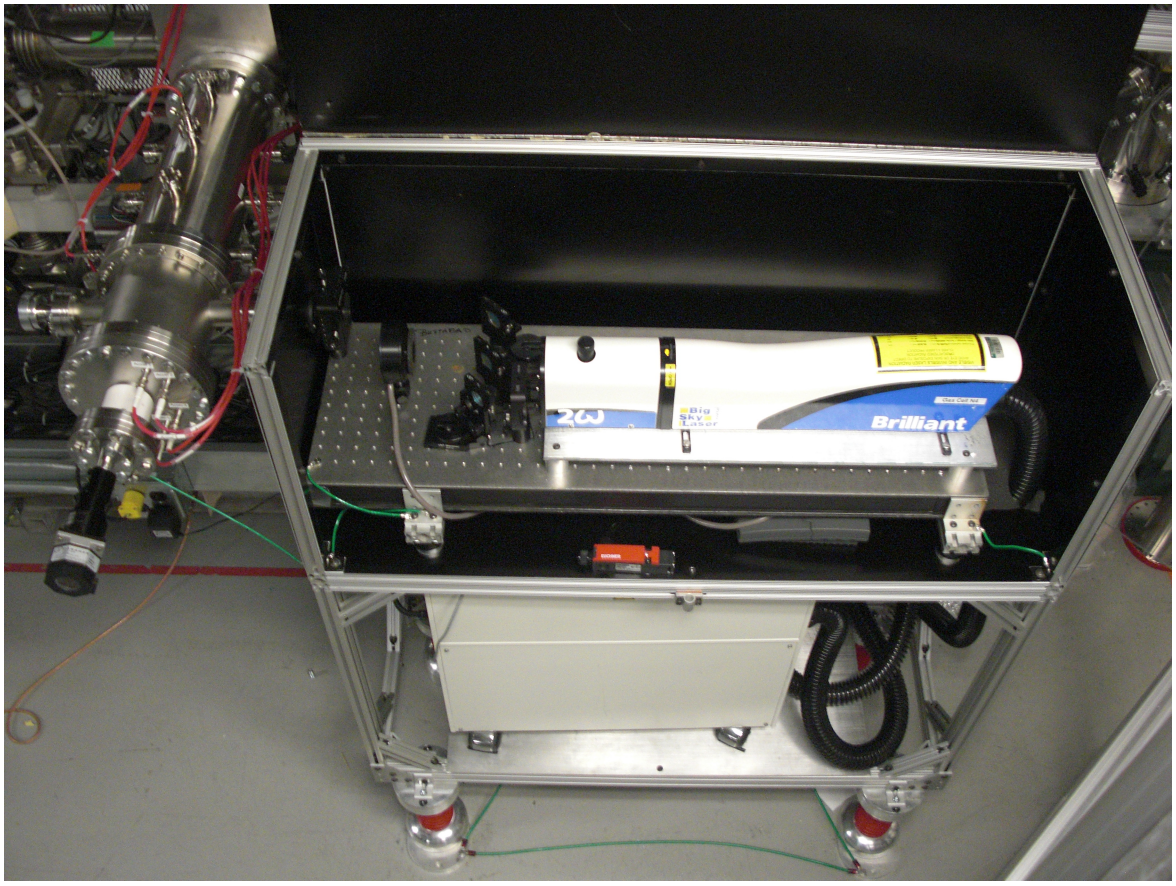

Figure 3.8: Overview of the laser ablation source. For this picture, the laser enclosure is open to show the laser head and the laser optics. The laser power supply is housed on the stand underneath the optical table. The red 60 kV insulators allow the laser system to run on a high voltage platform, which is required for LAS operation during rare isotope beam experiments.

is interlocked and connected to the laser power supply. If opened, the laser shuts off. The laser power supply is also located on the stand below the enclosure for the optical table. The laser stand is set on 60 kV insulators. Thus LAS can not only be used as a means of offline ion production but can also be used during experiments while operating on a 60 kV platform.

A small circular hole is cut into the enclosure panel next to the vacuum chamber in order for the laser light to propagate into the vacuum chamber. For the ∼30 mm between the aluminum enclosure and the vacuum chamber, the light is enclosed in an opaque light tunnel

constructed from Lexan that is painted black. To ensure that the tunnel is light tight, it is covered with black silicone rubber wrap from UZ Engineered Products. These materials were chosen to bridge the 5 kV potential difference from the laser enclosure to the LEBIT beamline before the buncher.

After the Lexan tunnel, the laser light enters vacuum via a 38.1 mm diameter optical window that is held by vacuum against the O-ring of a modified Klein Flange (KF) 25 centering ring. A custom aluminum holder was designed and fabricated in order to mount the in-vacuum prism that reflects the laser light to the target; see Fig. 3.9. The prism mount has a shallow triangular indent to ensure that the prism is oriented such that the laser light hits the target in the desired location and with a 18 degree angle of incidence. A RF finger provides the necessary tension on the prism to secure it in the triangular indent. A thin aluminum cover fits over the prism holder and helps prevent the prism from becoming coated. The cover has a 7 mm diameter hole so that the laser light can get out and be reflected to the target. Additional holes are placed along the holder on the side that is away from the

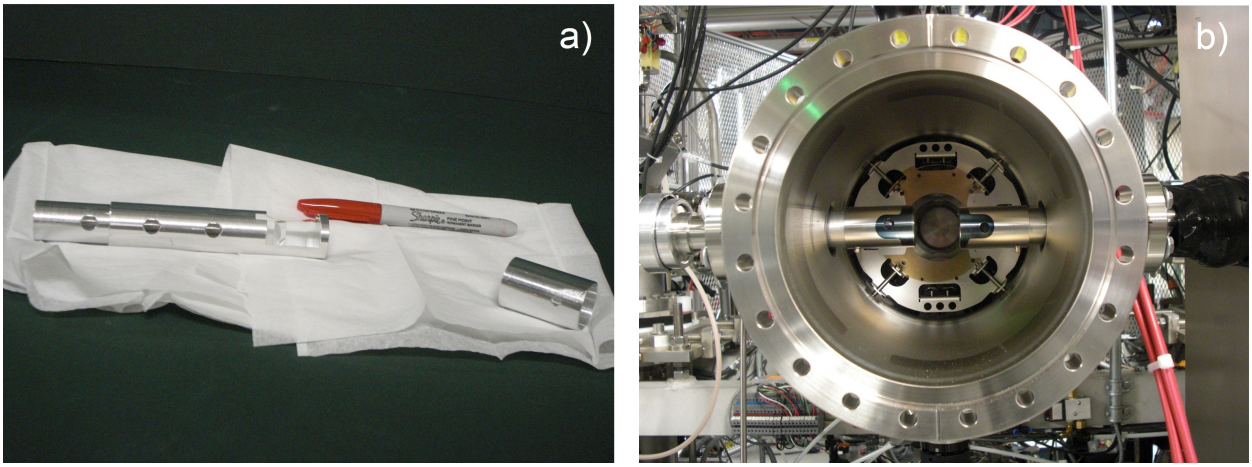

Figure 3.9: a) Prism mount with the cover removed to show the prism secured with a RF finger. A sharpie marker is included in the picture as a size reference. b) Prism mounts secured in the vacuum chamber and covered to prevent coating. The chamber view is from the target side; the laser enclosure is on the right side of the picture. The extraction system has been removed to better view the prism mounts.

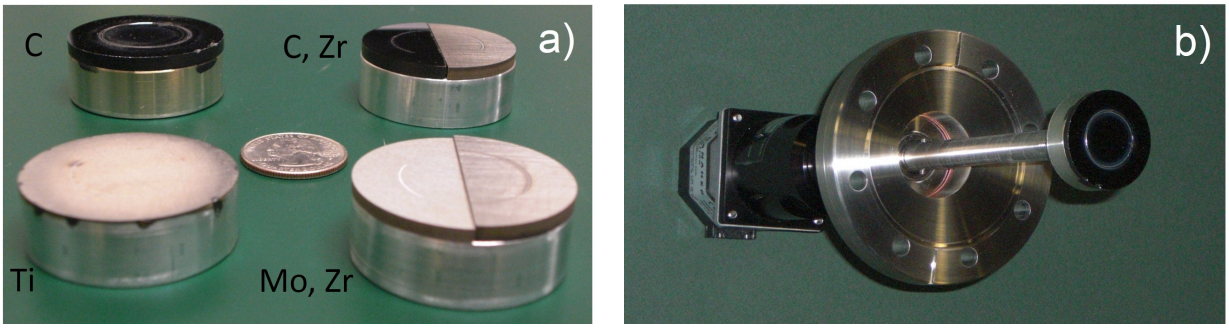

Figure 3.10: a) LAS ablation targets. The pictured targets include carbon and titanium single element targets as well as multi element targets of carbon, zirconium and molybdenum, zirconium. A U.S. quarter coin has been included in the picture for a size reference. b) Carbon target mounted to the rotation system. The offset between the rotary feedthrough and the center of the reducer flange can be seen in the picture. The 20 mm diameter circular track cut out by the laser when the target is rotated is visible.

target. These holes help prevent pockets of air from becoming trapped in the holder, and since they are located only on the side opposite the target, they do not compromise the shielding that helps keep the prisms from becoming coated.

3.3.2 Targets

LAS provides the capability to produce ions of many different elements, and the source has been designed to facilitate the transition between ion production of different elements. Targets are mounted using a method comprised of two main parts. First, all targets are mounted from a common stainless steel shaft. One side of the shaft connects to the rotary feedthrough, and the other is threaded for the mounting of the target. Second, for each target a 40 mm diameter aluminum cylinder with a height of typically 12.7 mm and a threaded through hole in the middle is fabricated. The target, generally 3 mm or thinner, is then glued to the aluminum mount using EPO-TEK 353ND-T. Gluing the target to the mount enables a flat target surface and helps ensure parallel extraction of ions. Thus, targets can easily be switched out by swapping aluminum mounts. Fig. 3.10 shows many different

Figure 3.11: a) Four ring LAS extraction system used to accelerate ions to 5 keV beam energy. b) Electrostatic quadrupole triplet for additional focusing before the 90 degree bend to the main LEBIT beamline.

targets that have been ablated with LAS.

For measurements where switching between selective ion production of different elements is preferable, a more sophisticated method has been developed that does not require breaking vacuum to switch out the target. This method uses multi element targets, a Powermax stepper motor, and a Kollmorgen driver which can be employed for selective rotation such that only the desired element is ablated. The switching process for multi element targets is incorporated into the LEBIT PLC system and is fully automated.

3.3.3 Ion Optics

In order to realize the ion optical elements that were shown effective in simulation, existing electrode structures were repurposed with slight modifications when required. An electrode structure [57] that had been used previously to accelerate ions from the gas cell stopping area to the LEBIT facility was modified for the LAS extraction system. Simulations indicated that the four ring system is sufficient and that the existing ring spacing is suitable for LAS purposes. The inner diameter of the extraction rings was expanded to 30 mm and small cutouts were added about the plane of incidence for the laser light. An electrostatic

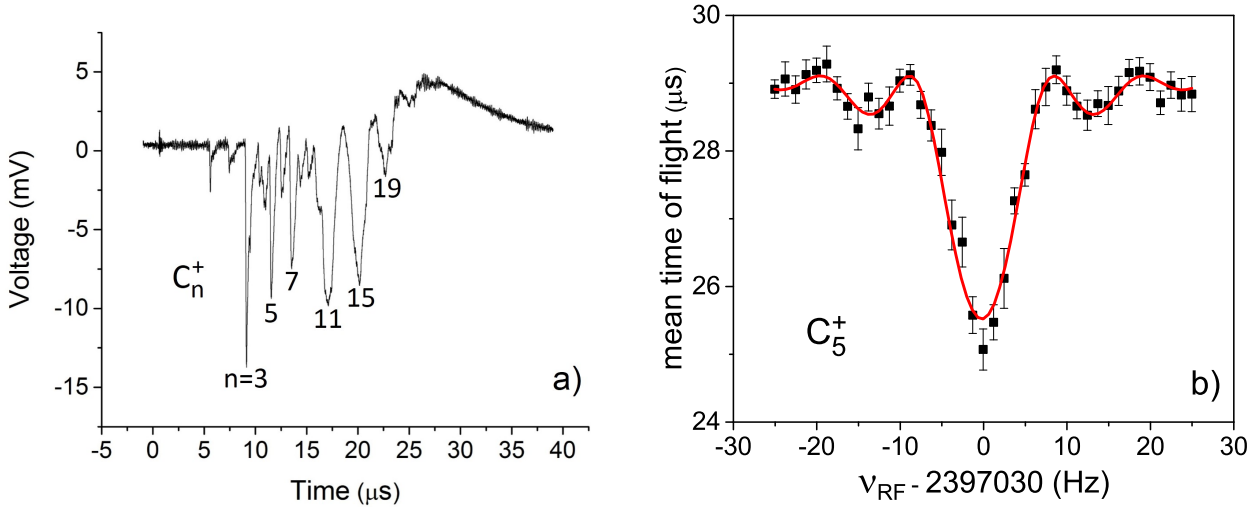

Figure 3.12: a) Spectrum of singly charged cluster ions of carbon-12 detected on a micro channel plate directly after the 90 degree bender. Ion peaks have been identified based on relative times of flight to the detector. b) Time of flight ion cyclotron resonance curve of C_5^+ ions that were produced via laser ablation. A traditional quadrupole excitation technique with an excitation time of 100 ms was used to form the resonance.

quadrupole triplet with a 55 mm inner diameter that was machined in Frankfurt was employed for additional focusing. The extraction system and quadrupole triplet are shown in Fig. 3.11. After ablation, this pair of optics is used for efficient transport to the main LEBIT beamline. The beam properties are sufficient to achieve acceptance into the cooler buncher [56] with the existing LEBIT ion optical elements after the 90 degree bender.

3.3.4 First Ions

With the laser optics, target rotational system, and ion optics realized, a Sigradur carbon target was ablated with LAS. Ions were searched for on a micro channel plate (MCP) located directly after the 90 degree bender. The first detection of ions produced by laser ablation at the LEBIT facility was accomplished February 12, 2013. One of the first spectra of singly charged cluster ions of carbon-12 is shown in Fig. 3.12 a), where ion peaks have been identified by relative times of flight. This spectrum is evidence of successful ion production

via laser ablation, as well as the successful extraction and transport of ions after ablation.

The carbon cluster ions produced by laser ablation were then accumulated in the ion cooler and buncher [56]. After preparation, the cooled bunches of ions were released toward the 9.4 T Penning trap system [58]. The desired carbon cluster ion was selected based on time of flight; all other cluster ions were removed using a pulsed electric steerer as a fast beam gate in the transport line to the trap. Several resonances of various carbon cluster ions were successfully obtained. One of the first carbon cluster resonances, taken in February of 2013, is shown in Fig. 3.12 b). This resonance demonstrates that Penning trap mass measurements of ions produced with the newly developed laser ablation source are possible.

Chapter 4

The laser ablation source for production of carbon cluster ions

4.1 Introduction and motivation

The set of cluster ions of ^{12}C is an extremely useful tool for a mass spectrometry facility. Carbon cluster ions have essentially no mass uncertainty by virtue of the definition of the atomic mass unit, u = $\frac{1}{12}$ m(^{12}C). In addition, the set of carbon cluster ions spans the entire nuclear chart in multiples of 12 u; see Fig. 4.1. Therefore carbon cluster ions offer a great opportunity to probe systematic effects. By comparing measured cyclotron frequency ratios of carbon cluster ions with known values throughout a broad mass range, mass-dependent systematic effects can be evaluated.

Similar cross reference measurements using carbon cluster ions have been performed at ISOLTRAP, SHITPTRAP, and JYFLTRAP [1, 2, 3]. In these studies, mass-dependent systematic effects were determined to lead to relative errors on the order of $\sim 10^{-10}$/u $\times$ m_{diff}, where m_{diff} is the mass difference between the two measured ions in atomic mass units.

Using carbon cluster ions produced with the newly developed laser ablation source, a study was conducted at the LEBIT facility to investigate if systematic effects are small and

on the order of those at other Penning trap facilities. The carbon cluster cross reference measurement and the resulting evaluation of LEBIT mass-dependent systematic effects are discussed in this chapter.

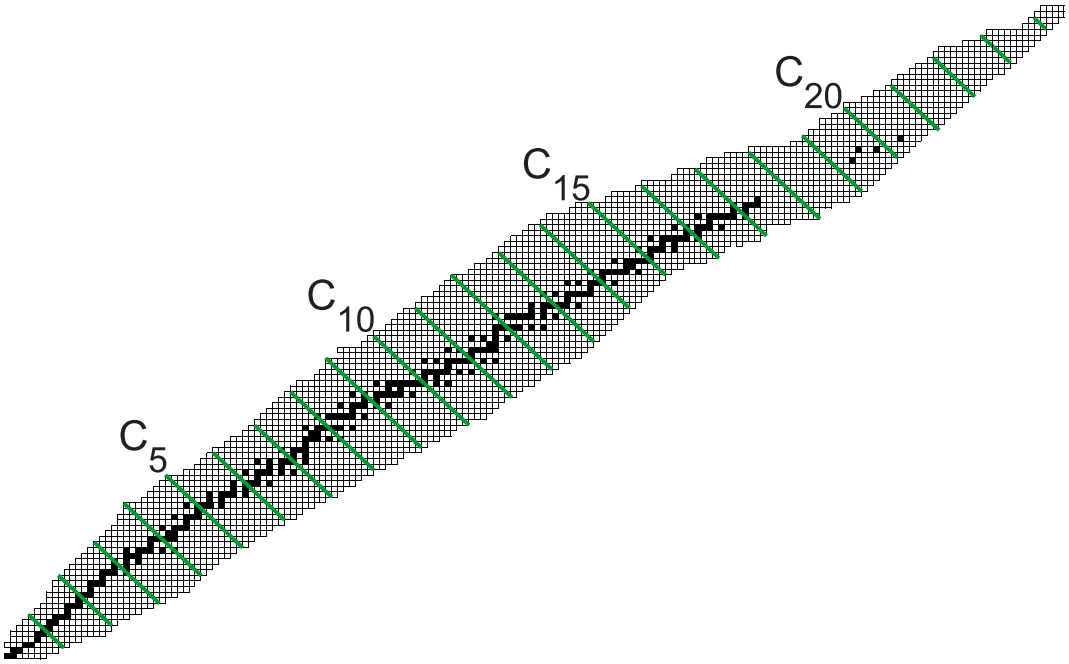

Figure 4.1: Nuclear chart overlaid with green lines to represent the multiple of 12 mass numbers that correspond to carbon clusters. The figure illustrates that carbon cluster ions span the entire nuclear chart, which makes them an ideal tool to probe systematic effects across a broad mass range.

4.2 Measurement Procedure

The laser ablation source was used to produce singly charged cluster ions of carbon-12 at the LEBIT facility. For an overview of the portion of LEBIT used in this measurement see Fig. 4.2. A Sigradur G carbon target was ablated with 532 nm laser light from a Nd:YAG laser. Relatively low laser pulse energies of $\sim$1 mJ were used to help prevent breakup of heavier carbon clusters ions. The carbon cluster ions were accelerated to 5 keV beam energy by means of a four ring extraction system and then focused with an electrostatic quadrupole

triplet. After the triplet, an electrostatic quadrupole deflector bent the ion beam 90 degrees onto the axis of the main LEBIT beamline. The ions were then transported electrostatically to the LEBIT ion cooler and buncher [56] where they were cooled for 30 ms via collisions with helium buffer gas. The ions were then bunched and released in microsecond pulses. In the transport line to the Penning trap, an electric steerer is used as a fast beam gate so that only the desired carbon cluster ion is captured in the LEBIT Penning trap [58].

Once the desired carbon cluster ion is captured in the Penning trap, a quadrupole RF electric field is applied following a Ramsey excitation method [68, 67, 69]. Two 150 ms bursts of RF were separated by a 450 ms period where no excitation was applied. The desired ion is then ejected and the time of flight to a downstream MCP detector is measured. This process is repeated with RF excitation frequencies near the cyclotron frequency of the ion. Over the course of roughly 30 minutes, a time of flight ion cyclotron resonance curve (described in more detail in Section 2.5.4) is built up, such as the example resonance in Fig. 4.3 for C_{12}^{+} ions. The data are fitted with a theoretical line shape [66, 68]; the central minimum in time of flight corresponds to the cyclotron frequency of the ion.

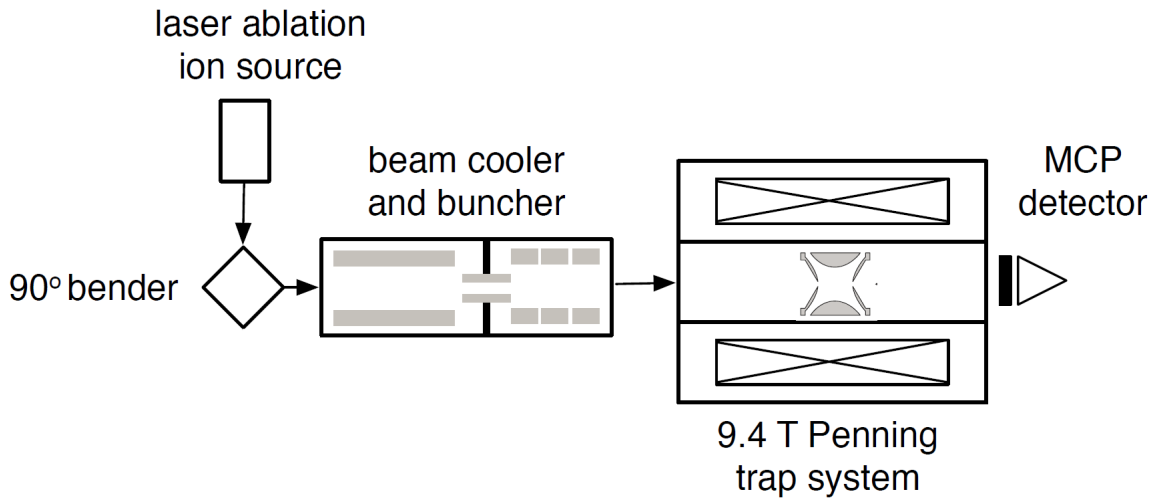

Figure 4.2: Overview of key components of the LEBIT facility used in the cross reference measurement with carbon cluster ions.

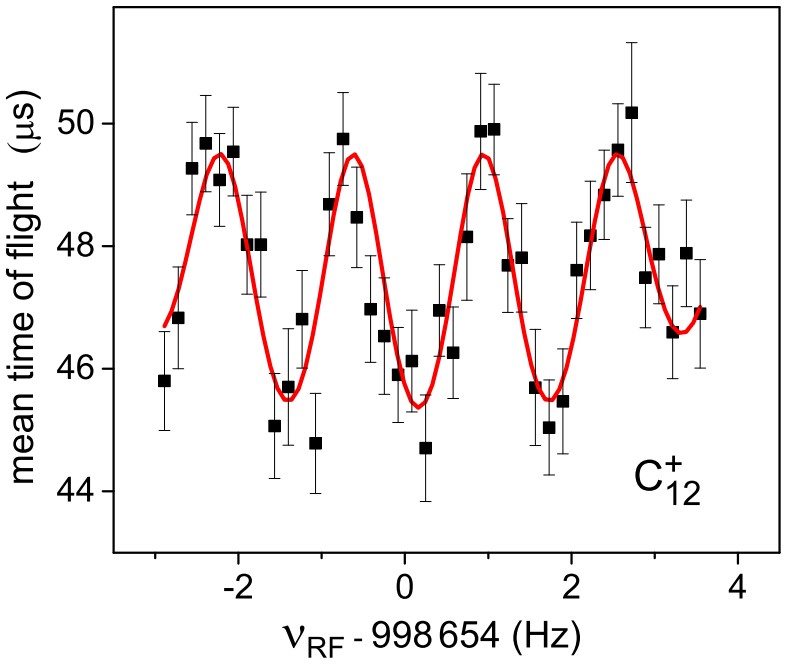

Figure 4.3: One of 101 time of flight ion cyclotron resonance curves of carbon cluster ions used to probe LEBIT systematic effects. This example resonance curve of C_{12}^+ ions was obtained using a Ramsey excitation technique. The characteristic Ramsey fringes [68] were fitted, and the cyclotron frequency of the ion, given by the minimum of the central trough, was determined.

In this investigation, three different carbon clusters, C_6^+, C_9^+, and C_{12}^+, were measured with C_3^+ as a reference. Resonances of C_6^+, C_9^+, and C_{12}^+ were cycled through while interweaving reference resonances of C_3^+. Thus the resonance order was C_3^+, C_6^+, C_3^+, C_9^+, C_3^+, C_{12}^+, C_3^+ etc. The bracketing pairs of C_3^+ resonances were then linearly interpolated to determine the cyclotron frequency of C_3^+ at the time of the resonance of the ion of interest, either C_6^+, C_9^+, or C_{12}^+. In this manner cyclotron frequency ratios of $\nu_c(C_3^+)/\nu_c(C_6^+)$, $\nu_c(C_3^+)/\nu_c(C_9^+)$, and $\nu_c(C_3^+)/\nu_c(C_{12}^+)$ were obtained.

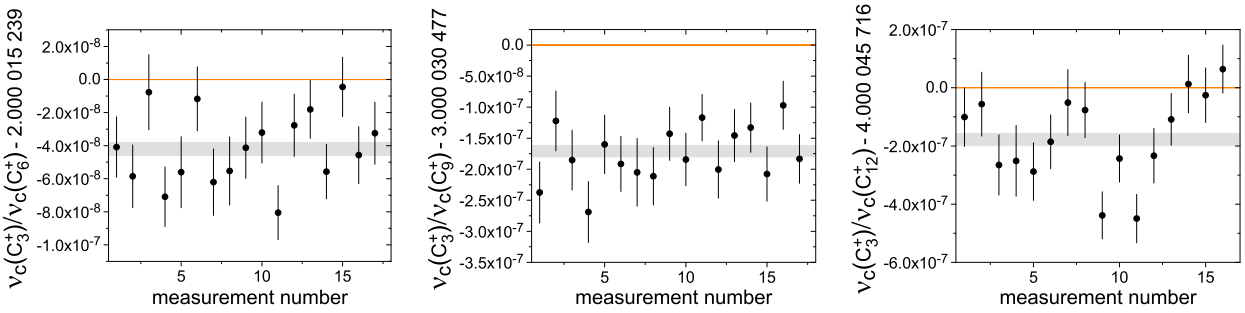

Figure 4.4: Measured cyclotron frequency ratios of $\nu_c(C_3^+)/\nu_c(C_6^+)$, $\nu_c(C_3^+)/\nu_c(C_9^+)$, and $\nu_c(C_3^+)/\nu_c(C_{12}^+)$ compared with the true cyclotron frequency ratio (orange solid line). The error bars represent the statistical uncertainty of each cyclotron frequency ratio measured. The mean value and corresponding 1σ uncertainty of each data set is denoted by the gray shaded bar.

4.3 Results

Over the course of three days 101 time of flight ion cyclotron resonance curves were measured. Roughly 1 000 to 2 000 ions were detected for each resonance, where only events with five or fewer detected ions were considered. From the time of flight ion cyclotron resonance curves, a total of 50 cyclotron frequency ratios were obtained. The collection of cyclotron frequency ratios is presented in Fig. 4.4. The Birge ratio [77], i.e. the ratio of the probable error based on internal consistency to that based on external consistency, for each of the three data sets, $\nu_c(C_3^+)/\nu_c(C_6^+)$, $\nu_c(C_3^+)/\nu_c(C_9^+)$, and $\nu_c(C_3^+)/\nu_c(C_{12}^+)$, is 1.21(12), 1.04(12), and 1.71(12) respectively. The greater than unity Birge ratios, especially for the case of the $\nu_c(C_3^+)/\nu_c(C_{12}^+)$ data set, indicate that the statistical uncertainty does not adequately take into account systematic effects. In order to compensate for the greater than statistical fluctuations of the data, the statistical uncertainty of the weighted average of each data set was scaled by the respective Birge ratio. For more information about the Birge ratio and the LEBIT analysis methodology refer to [59]. The resulting determinations of the cyclotron frequency ratios are listed in Table 4.1. The measured cyclotron frequency ratios

Table 4.1: Measured cyclotron frequency ratios (with listed statistical errors) compared with the true cyclotron frequency ratio of the carbon cluster ions. The relative error of each cyclotron frequency ratio $\varepsilon(r)/r$ is listed.

Ratio	True	Measured	$\varepsilon(r)/r \times 10^{-8}$
$\nu_c(C_3^+)/\nu_c(C_6^+)$	2.000 015 239	2.000 015 197(5)	-2.10 (27)
$\nu_c(C_3^+)/\nu_c(C_9^+)$	3.000 030 477	3.000 030 306(11)	-5.69 (37)
$\nu_c(C_3^+)/\nu_c(C_{12}^+)$	4.000 045 716	4.000 045 538(24)	-4.4 (1.0)

were compared with the true ratios, and the relative error of each cyclotron frequency ratio $\varepsilon(r)/r$ was calculated. The uncertainty of the weighted average of each data set, after being scaled by the Birge ratio, was then propagated to determine the uncertainty of $\varepsilon(r)/r$. The relative errors of the cyclotron frequency ratios and the corresponding uncertainties are presented in Table 4.1 as well.

The obtained values of $\varepsilon(r)/r$ were plotted as a function of the mass difference between the measured carbon cluster ion and the C_3^+ reference; see Fig. 4.5. In order to determine the overall result of mass-dependent systematic effects, a weighted linear fit of the data that was constrained to pass through the origin was performed. The slope of the fit helps quantify the effect of mass-dependent systematics and is given by -6.7(1.0) $\times 10^{-10}$/u.

4.4 Discussion

As expected in this measurement with such an enormous mass range, mass-dependent systematic effects lead to frequency shifts greater than the statistical uncertainty of the measurement. Examples of mass-dependent systematic effects include Penning trap imperfections such as deviations from a purely quadrupole electric potential and trap misalignment with respect to the magnetic field [4]. Since only events with five or fewer detected ions were considered, any effects due to multiple ions in the trap are negligible compared to other

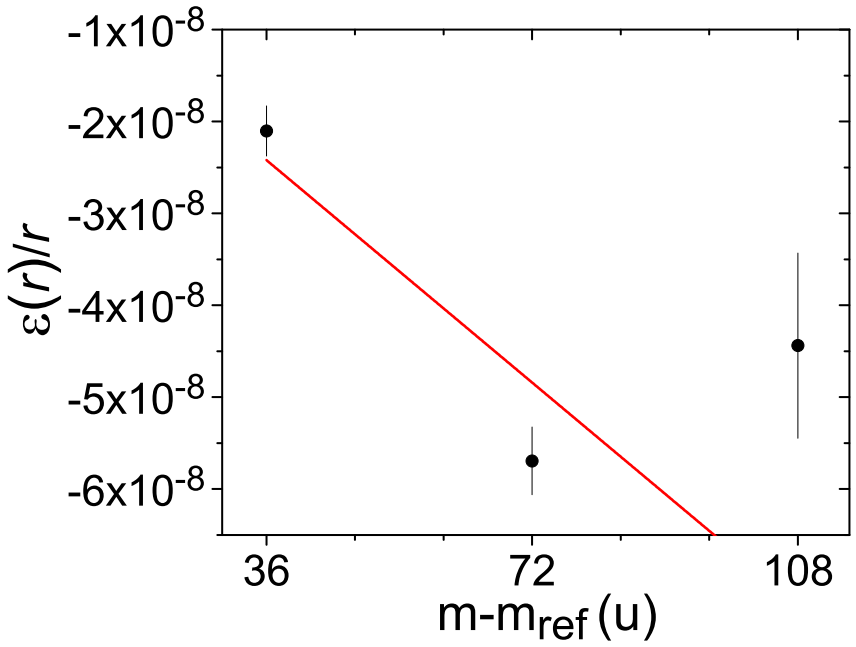

Figure 4.5: Relative error $\varepsilon(r)/r$ of measured cyclotron frequency ratios of carbon cluster ions plotted as a function of the mass difference between the measured carbon cluster ion and the C_3^+ reference. The statistical uncertainty of each cyclotron frequency ratio was scaled by the Birge ratio [77] of the data set; the error bars of the $\varepsilon(r)/r$ data points are reflective of this scaling. The red line denotes a linear weighted fit of the data that was constrained to pass through the origin and has a slope of -6.7(1.0) $\times$ 10^{-10}/u.

mass-dependent systematic effects. Although to first order mass-dependent systematic effects lead to relative errors that are proportional to the mass difference between measured ions [4], higher order effects can arise for example due to differences in the amplitudes of the reduced cyclotron, magnetron, and axial motions. Such differences could be the result of slightly different capture in the Penning trap from the different ion cooler and buncher [56] RF amplitudes that were applied in the measurement. Adjusting the RF settings for the buncher was required for transmission across such a vast mass range. In consideration of the large mass range of the measurement and the results of similar measurements at other Penning trap facilities [1, 2, 3], the deviation from linearity is not surprising. The results support that higher order effects become more pronounced with a large mass difference between measured ions.

The determination of mass-dependent systematic effects from this study can be used to assign an appropriate uncertainty in future measurements. Also, in the future, additional carbon cluster cross reference measurements could even be performed while adjusting in place trap correction parameters [58] in order to minimize these mass-dependent systematic effects. Nonetheless, for all cases in this work, even for the case with a mass difference of 108 u, the relative error in the cyclotron frequency ratio is on the order of 10^{-8}, which corresponds to a relative shift of $\sim 10^{-10}$/u. These results show that LEBIT mass-dependent effects are small and are comparable to those of other Penning trap facilities [1, 2, 3].

Chapter 5

First Direct Determination of the ^{48}Ca Double Beta Decay Q Value

5.1 Experimental Procedure of the ^{48}Ca Double Beta Decay Q Value Measurement

The first direct measurement of the ^{48}Ca double beta decay Q value was accomplished at the LEBIT facility in 2013 [78]. Ions for the measurement were produced by the tandem operation of a modified commercial ion source from Colutron Research Corporation and the recently commissioned laser ablation ion source. Calcium ions were produced with the Colutron source via surface ionization, as in the previous LEBIT atomic mass measurement of ^{48}Ca [48]. A cylindrical ceramic holder containing ∼50 mg of granular calcium was inserted into a tungsten filament coil. The filament was heated, emitting electrons and producing calcium vapor. Calcium ions were produced by biasing the filament to around 100 V. The laser ablation source, opposite the Colutron source and perpendicular to the LEBIT beamline, was used to produce titanium ions; see Figure 5.1. (The laser ablation ion source is described in detail in Chapter 3.) A thin, 40 mm diameter circular titanium target was glued to an aluminum mount and rotated with a stepper motor. Titanium ions were produced by bombarding the target with ∼1 mJ of pulsed 532 nm light from a Nd:YAG

laser. Switching between measurements of calcium and titanium ions was done by reversing the polarity of the electrostatic quadrupole bender, which determines whether ions from the laser ion source or the Colutron ion source were sent down stream to the beam cooler and buncher [56]. After preparation in the cooler-buncher, cooled ion bunches of the desired element were sent in microsceond ion pulses to the Penning trap. In the transport line to the trap, isotopes with mass number other than A = 48 were removed with a pulsed electric steerer based on the time of flight from the cooler-buncher. Pure samples of either $^{48}Ca^{+}$ or $^{48}Ti^{+}$ were then captured in the 9.4 T LEBIT Penning trap [58].

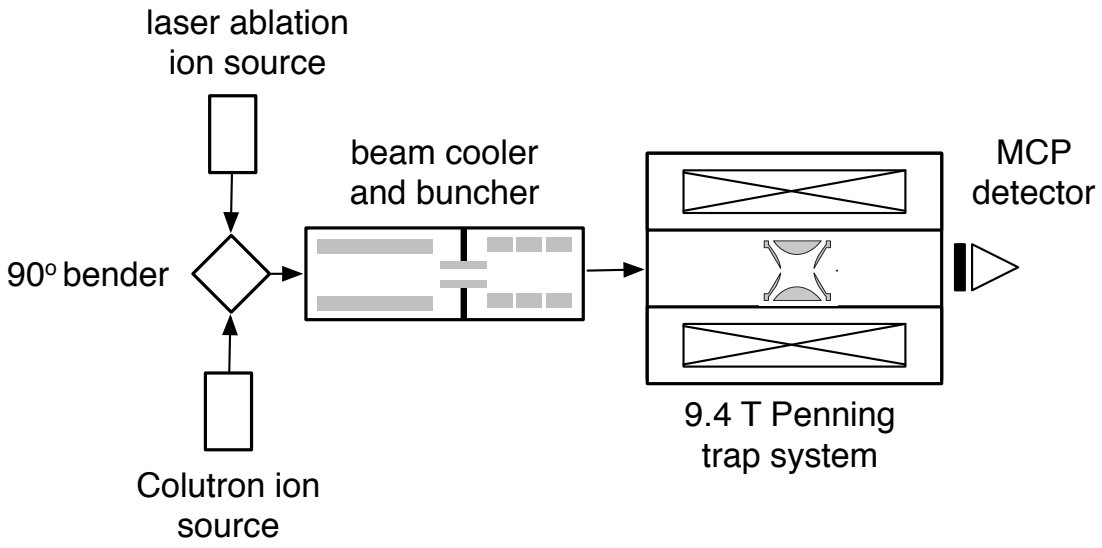

Figure 5.1: Schematic overview of the main components of the LEBIT facility used in the direct measurement of the ^{48}Ca double beta decay Q value.

5.2 Experimental Results and Error Analysis

The cyclotron frequencies of $^{48}Ca^{+}$ and $^{48}Ti^{+}$ ions were determined using a time of flight ion cyclotron resonance detection technique, as described in section 2.5.4. For this measurement, a total of 88 cyclotron frequency measurements were taken in a period of two weeks. Resonances were formed in approximately 30 minutes, and approximately 400 to 2000 ions

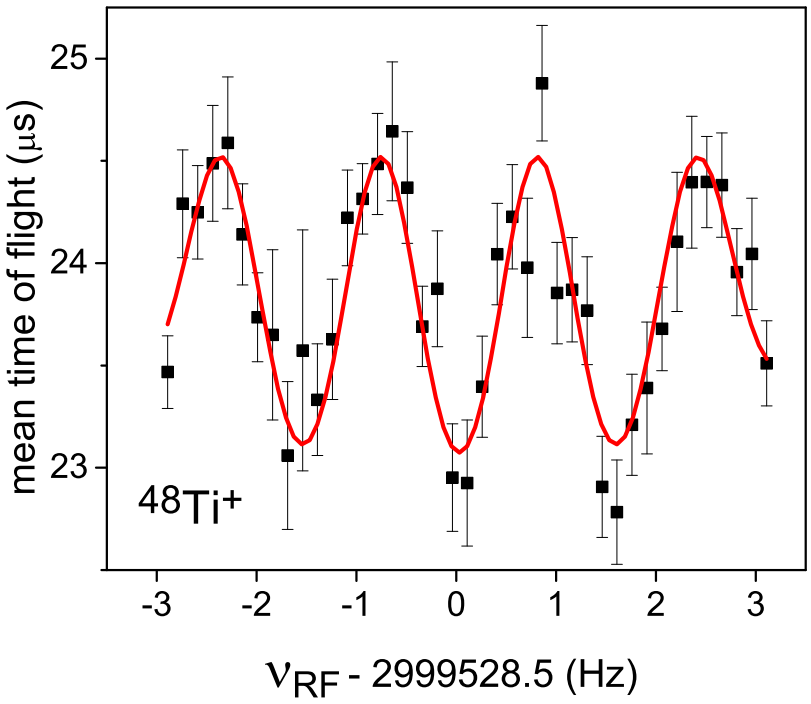

Figure 5.2: An example time of flight ion cyclotron resonance curve from the collection of 88 resonances used in the measurement of the ^{48}Ca double beta decay Q value. This resonance of $^{48}Ti^{+}$ ions was formed using a Ramsey excitation technique. The theoretical line shape [66] from fitting the experimental data is represented by the red solid line. The minimum of the central trough corresponds to the cyclotron frequency of $^{48}Ti^{+}$.

were detected for each resonance. Two different excitation schemes were employed. A Ramsey excitation scheme [68, 67, 69] was used in 49 resonances, and a traditional quadrupole excitation technique [66] was used in 39 resonances. A typical Ramsey resonance is shown in Figure 5.2. For the Ramsey resonances, two 150 ms RF bursts were separated by a 450 ms wait. For the traditional quadrupole resonances one continuous 750 ms burst of RF was applied. Note that the total time in the trap for both excitation techniques is the same.

Each resonance was fitted and the corresponding theoretical line shape [66] was used to determine the cyclotron frequency of the ion, either $^{48}Ca^{+}$ or $^{48}Ti^{+}$. To determine the cyclotron frequency ratio $\nu_c(^{48}Ca^{+})/\nu_c(^{48}Ti^{+})$, resonances of $^{48}Ti^{+}$ were taken both before and after every $^{48}Ca^{+}$ resonance. Bracketing pairs of $^{48}Ti^{+}$ resonances were then

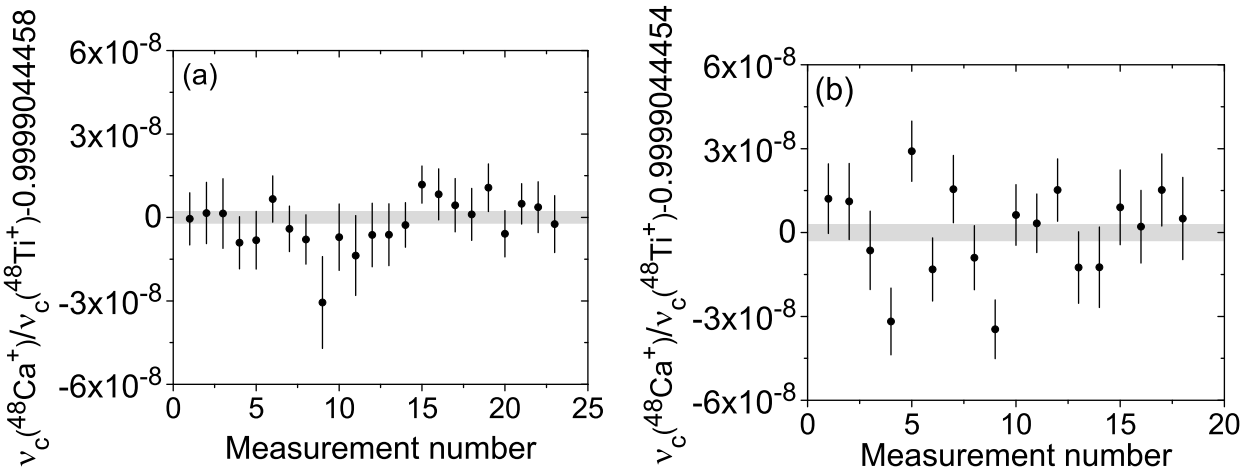

Figure 5.3: Collection of cyclotron frequency ratios of $^{48}Ca^+$ and $^{48}Ti^+$, $\nu_c(^{48}Ca^+)/\nu_c(^{48}Ti^+)$. For the data set presented in (a) a Ramsey excitation scheme was used, and in (b) a traditional quadrupole excitation scheme was used. Each collection is centered around the mean value. The error bars represent the statistical uncertainty of each cyclotron frequency ratio, and the shaded bar denotes the 1σ statistical uncertainty of the mean value.

linearly interpolated to determine the cyclotron frequency of $^{48}Ti^+$ at the time of the $^{48}Ca^+$ resonance. The resulting 41 cyclotron frequency ratios are plotted in Fig. 5.3, where a Ramsey and traditional quadrupole excitation technique were used in the data sets presented in (a) and (b) respectively. The mean values from the two data sets agree well. The mean of the Ramsey excitation data set is $\nu_c(^{48}Ca^+)/\nu_c(^{48}Ti^+) = 0.999\ 904\ 445\ 8(20)$ and the mean of the traditional quadrupole excitation is $\nu_c(^{48}Ca^+)/\nu_c(^{48}Ti^+) = 0.999\ 904\ 445\ 4\ (29)$. The uncertainty associated with the mean cyclotron frequency ratio of each data set is statistical. The Birge ratio [77] for data sets (a) and (b) are 0.84 (10) and 1.47 (11) respectively. These results are given in Table 5.1.

In this measurement, known systematic sources of errors lead to an error much less than the statistical uncertainty. Obtaining $\nu_c(^{48}Ca^+)/\nu_c(^{48}Ti^+)$ directly in a mass doublet measurement practically eliminates mass-dependent systematic effects. The steady ion production from the Colutron and laser ablation ion sources enabled sufficient statistics to

Table 5.1: Mean cyclotron frequency ratio $\nu_c(^{48}Ca^+)/\nu_c(^{48}Ti^+)$ obtained from each data set with the excitation technique, statistical uncertainty, and the Birge ratio [77] listed. The overall experimental result, weighted average of the two data sets, is also presented

Excitation	$\sigma_{stat} \times 10^{-9}$	Birge Ratio	Ratio
Ramsey	2.0	0.84 (10)	0.999 904 4458(20)
Quadrupole	2.9	1.47 (11)	0.999 904 4454(42)
Average			0.999 904 4457(18)

obtain a cyclotron frequency ratio in ∼1 hour. In this time period nonlinear magnetic field fluctuations are negligible for the obtained precision [33]. Ion production via two independent sources was ideal for ensuring the purity of samples in the Penning trap. During $^{48}Ti^+$ resonances, the electrostatic quadrupole bender directed all $^{48}Ca^+$ ions upstream away from the cooler-buncher, and vice versa. The purity of both $^{48}Ti^+$ and $^{48}Ca^+$ samples was checked by setting the frequency of a dipole RF field [61, 4] to drive out the desired ion and verifying that no counts were detected on the MCP i.e. no contaminant ions were present in the trap. Since there were no trapped contaminant ions, there was no systematic error due to Coulomb interaction with impurities in the trap. Nonetheless as an additional safeguard, only events with five or fewer detected ions were considered. Note this limit did not significantly alter the statistics of the measurement because the vast majority of events had five or fewer detected ions.

Even though all known systematic effects are negligible compared to the statistical uncertainty, for the traditional quadrupole excitation data set where the Birge ratio was greater than unity, the statistical error was scaled by the Birge ratio to account for any residual unknown systematic effects and nonstatistical fluctuations. The overall experimental result was then obtained from the weighted average of the two data sets:

$\nu_c(^{48}Ca^+)/\nu_c(^{48}Ti^+) = 0.999\ 904\ 445\ 7\ (18)$.

5.3 Determination of the Q Value and phase space factors of double beta decay in ^{48}Ca

The 2013 LEBIT measurement of $\nu_c(^{48}\mathrm{Ca}^+)/\nu_c(^{48}\mathrm{Ti}^+)$ was used to provide the first direct determination of the ^{48}Ca double beta decay Q value. The Q value can be expressed in terms of the cyclotron frequency ratio (inverse mass ratio).

$$Q_{\beta\beta} = \Big[m(^{48}\mathrm{Ca}) - m_e\Big]\left[1 - \frac{\nu_c(^{48}\mathrm{Ca}^+)}{\nu_c(^{48}\mathrm{Ti}^+)}\right]c^2, \tag{5.1}$$

where m(^{48}Ca) is the atomic mass of ^{48}Ca, m_e is the electron mass, and c is the speed of light. Using the measured cyclotron frequency ratio and the 2012 AME [7] value of the atomic mass of ^{48}Ca yields $Q_{\beta\beta} = 4268.121\ (79)$ keV. This new determination indicates an increase of 1.2 keV, a shift of 3 σ, from the Q value calculated using 2012 AME masses. The uncertainty of $Q_{\beta\beta}$ has also been improved by a factor of five via the direct measurement at the LEBIT facility. Note that for the obtained precision, $Q_{\beta\beta}$ in Eq. 5.1 is insensitive to the value used for $m(^{48}\mathrm{Ca})$ to within several keV.

The 2013 LEBIT measurement of the ^{48}Ca double beta decay Q value was applied in an improved determination of the phase-space factors $G_{2\nu}$ and $G_{0\nu}$ for the two and zero neutrino modes of double beta decay in calcium-48. For the calculation, the procedure described in Ref. [79] was followed with a weak interaction axial-vector coupling constant of $g_A = 1.254$. The resulting phase space factors are 0.3% and 0.1% different from $G_{2\nu}$ and $G_{0\nu}$ computed in Ref. [48], which relied on the AME 2011 atomic mass value of ^{48}Ti for the calculation of $Q_{\beta\beta}$. With the direct determination of the Q value, the uncertainty in both $G_{2\nu}$ and $G_{0\nu}$ has now been reduced by a factor of 6. These values are presented in Table 5.2.

Table 5.2: ^{48}Ca Double beta decay Q value from the direct measurement of $\nu_c(^{48}Ca^+)/\nu_c(^{48}Ti^+)$. The corresponding two and zero neutrino phase space factors have been calculated and are also presented.

Q value (keV)	$G_{2\nu}$ ($\times 10^{-17}$ yr^{-1})	$G_{0\nu}$ ($\times 10^{-14}$ yr^{-1})
4268.121(79)	3.936 9(7)	6.509 2(5)

Very recently the ^{48}Ca double beta decay Q value was determined by a direct measurement using the TITAN Penning trap mass spectrometer at TRIUMF [42]. The result is in excellent agreement with that of the 2013 measurement at LEBIT. The confirmation by a second, independent Penning trap measurement is a welcomed result.

The ^{48}Ca double beta decay Q value from the 2013 LEBIT measurement is plotted in Fig. 5.4 with other determinations for comparison. The LEBIT result, with a precision of better than 80 eV, is the most precise result to date and is over a factor of 4 more precise than any other determination.

5.4 Improved Determination of the Atomic Mass of ^{48}Ti

The atomic mass of ^{48}Ca was previously determined directly by Penning trap mass spectrometry at the LEBIT facility [48]. This high-precision measurement is 99.9% of the influence of the 2012 AME value of $m(^{48}Ca)$ [27, 7]. In the 2012 evaluation, the uncertainty of the atomic mass of ^{48}Ti, 400 eV, is over three times the uncertainty of $m(^{48}Ca)$. Moreover, $m(^{48}Ti)$ was largely determined indirectly; 89% of the influence is from the ^{47}Ti(n,γ)^{48}Ti reaction, which is based on the 1984 measurement reported in Ref. [80]. More recently at ISOLTRAP during an experimental run, the accuracy of the setup was checked with stable isotopes including

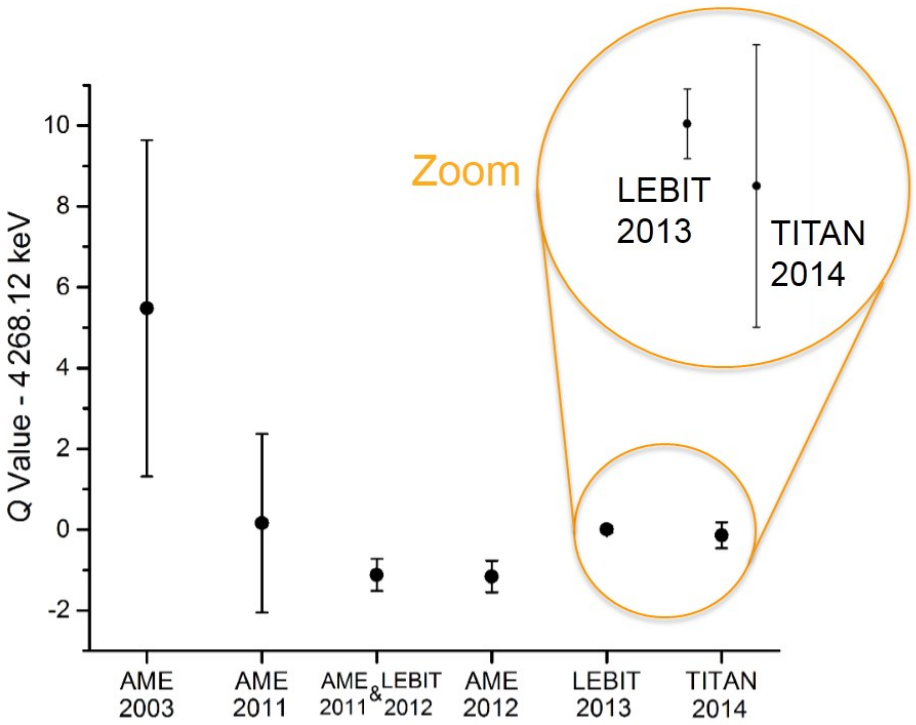

Figure 5.4: Determinations of the ^{48}Ca double beta decay Q value from the last 12 years. Plotted are the recent direct determinations using Penning trap mass spectrometry at the LEBIT facility in 2013 [78] and at the TITAN facility in 2014 [42]. Also plotted are determinations of the Q value based on the atomic masses in previous editions of the Atomic Mass Evaluation (AME) [7, 49]. The central point illustrates the determination based on a 2012 LEBIT measurement [48] of the atomic mass of ^{48}Ca together with the atomic mass of ^{48}Ti taken from the unpublished update to the AME in 2011 [50].

checks with molecular forms of ^{48}Ti. The average value from the ISOLTRAP cyclotron frequency ratios [81] of $m(^{48}\mathrm{Ti}^{16}\mathrm{O}^{+})/m(^{85}\mathrm{Rb}^{+})$ and $m(^{48}\mathrm{Ti}^{16}\mathrm{O}^{+})/m(^{55}\mathrm{Mn}^{+})$, albeit with a large uncertainty, contributes to the 2012 AME value of the $m(^{48}\mathrm{Ti})$ but differs by over 1 σ from the overall average value reported in the evaluation.

To help resolve the atomic mass of ^{48}Ti, the cyclotron frequency ratio $\nu_c(^{48}\mathrm{Ca}^{+})/\nu_c(^{48}\mathrm{Ti}^{+})$ measured at the LEBIT facility was used in conjunction with the 2012 AME [7] value of $m(^{48}\mathrm{Ca})$ to yield a new determination: $m(^{48}\mathrm{Ti}) = 47.947\ 940\ 75(16)$ u, which corresponds to a mass excess of -48 492.88(14) keV. The LEBIT determination of $m(^{48}\mathrm{Ti})$ agrees well with the ISOTRAP mass values [81], and the uncertainty has been reduced by a factor of

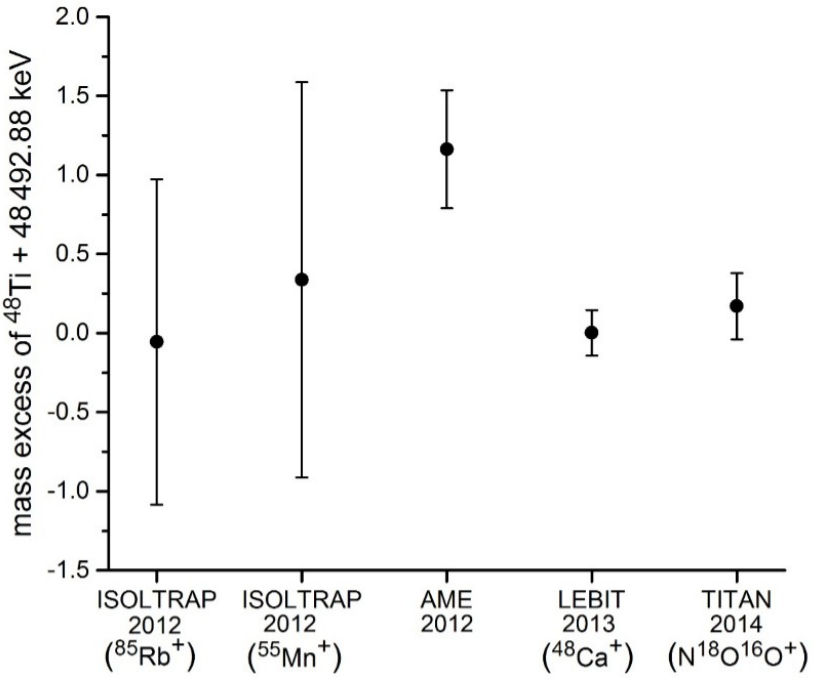

Figure 5.5: Comparison of mass excess values of ^{48}Ti from recent Penning trap measurements with AME 2012 [7]. For the Penning trap measurements, the mass used as a reference is noted in parenthesis.

five from the weighted average of the ISOTRAP measurements. The recent Penning trap measurements at LEBIT and ISOLTRAP indicate that ^{48}Ti is 1.2 keV more bound than what was reported in AME 2012, a shift of 3 σ. In consideration of these Penning trap measurements, we concluded in 2013 [78] that the reported shift in the ^{48}Ca double β decay Q value from AME 2012 is due to an error in the previously accepted value of $m(^{48}\mathrm{Ti})$. Very recently, this was confirmed by a direct Penning trap measurement of the atomic mass of ^{48}Ti by TITAN [42] using $\mathrm{N}^{18}\mathrm{O}^{16}\mathrm{O}^+$ as a reference mass. Fig. 5.5 shows the Penning trap measurements of $m(^{48}\mathrm{Ti})$ and compares them with the 2012 AME value. The 2013 determination of the atomic mass of ^{48}Ti at the LEBIT facility is still the most precise determination to date.

Chapter 6

Examination of the Possible Enhancement of Neutrinoless Double Electron Capture in ^{78}Kr

6.1 ^{78}Kr Double-electron capture Q value measurement procedure and results

A direct, Penning trap measurement of $\nu_c(^{78}Se^+)/\nu_c(^{78}Kr^+)$ was performed at the LEBIT facility in order to provide a better determination of the ^{78}Kr double-electron capture Q value. A schematic of the portion of the LEBIT facility used for the measurement is shown in Figure 6.1; see Ref [58] for a detailed description of the facility. For the measurement, a plasma ion source was used to simultaneously produce singly charged ions of $^{78}Kr^+$ and $^{78}Se^+$. Krypton doped helium support gas was introduced to the source via a needle valve, and ∼200 mg of granular selenium was loaded in a ceramic holder, which was inserted into the tungsten filament coil of the ion source. The filament was heated, emitting electrons and vaporizing the selenium. The filament was also biased at roughly 100 V to produce a discharge that ionized the krypton and selenium. The ratio of $^{78}Kr^+$ to $^{78}Se^+$ was balanced

to within roughly a factor of five by adjusting parameters of the ion source including the pressure of the support gas, the amount of krypton in the support gas, the filament heating, and the extent that the selenium holder was inserted into the filament coil.

After ion production, helium ions, initially the dominant component of the beam, were removed in the compact, mass-dependent radio frequency quadrupole (RFQ) ion guide system. The krypton and selenium ions were then guided electrostatically to the LEBIT RFQ cooler and buncher [56] for the preparation of cooled ion bunches. These bunches were then released to the 9.4 T LEBIT Penning trap mass spectrometer [58]. In the transport line to the Penning trap, ions with mass number other than A = 78 were removed with an electric steerer that was operated as a fast beam gate. Both $^{78}Kr^{+}$ and $^{78}Se^{+}$ ions were then captured in the Penning trap. After capture, a 100 millisecond dipole RF electric field [61, 4] was applied at the reduced cyclotron frequency of $^{78}Se^{+}$ to drive it out of the trap in order to prepare pure $^{78}Kr^{+}$ samples, and vice versa for the preparation of pure samples of $^{78}Se^{+}$. Once the samples were purified, the time of flight ion cyclotron resonance technique, as described in section 2.5.4, was employed using a quadrupole excitation of 750 ms. An example resonance is shown in Fig. 6.2 (a). Each resonance was formed in roughly 30 minutes,

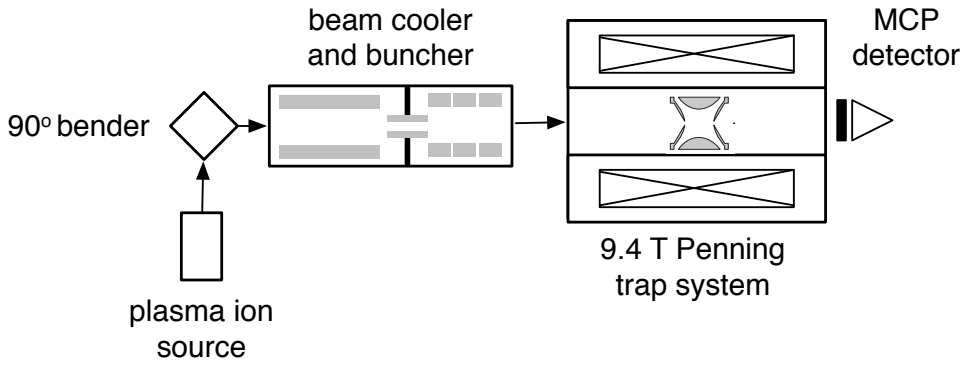

Figure 6.1: Schematic of the portion of the Low-Energy Beam and Ion Trap (LEBIT) facility used for the direct measurement of the cyclotron frequency ratio of $^{78}Se^{+}$ and $^{78}Kr^{+}$, $\nu_c(^{78}Se^{+})/\nu_c(^{78}Kr^{+})$.

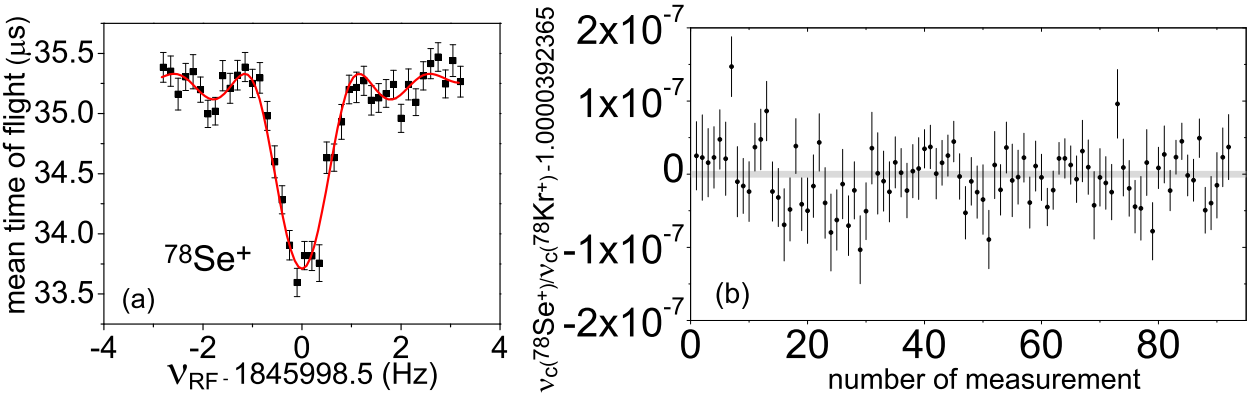

Figure 6.2: (a) An example $^{78}Se^{+}$ time of flight ion cyclotron resonance curve obtained using a 750ms quadrupole excitation technique. The theoretical line shape (red solid line) obtained from fitting the experimental data is used for the determination of the cyclotron frequency of the ion. (b) The collection of 92 cyclotron frequency ratios, about the mean value, used for the determination of $\nu_c(^{78}Se^{+})/\nu_c(^{78}Kr^{+})$. The error bars represent the statistical uncertainty of each ratio, and the gray shaded bar denotes the 1σ statistical uncertainty of the mean value.

and 400 to 2000 ions were detected for each resonance. Every $^{78}Kr^{+}$ resonance was flanked both before and after by a $^{78}Se^{+}$ resonance, which were linearly interpolated to determine the cyclotron frequency of $^{78}Se^{+}$ at the time of the $^{78}Kr^{+}$ resonance. This procedure was followed to obtain the cyclotron frequency ratio, $\nu_c(^{78}Se^{+})/\nu_c(^{78}Kr^{+})$.

A total of 209 resonances of $^{78}Kr^{+}$ and $^{78}Se^{+}$ were taken over the course of two weeks. From the 209 resonances, 92 cyclotron frequency ratios were obtained; these ratios are presented in Figure 6.2 (b). A weighted average of the 92 cyclotron frequency ratios was performed to yield the experimental result for the cyclotron frequency ratio:

$$\nu_c(^{78}Se^{+})/\nu_c(^{78}Kr^{+}) = 1.000\ 039\ 236\ 5\ (37).$$

6.2 Error analysis

The 3.7×10^{-9} uncertainty of the cyclotron frequency ratio is statistical. In this measurement, any systematic error is much less than the statistical uncertainty. Most systematic

effects (such as Penning trap electric field imperfections, misalignment of the trap with respect to the magnetic field, etc.) are proportional to the mass difference between measured ions, m_{diff} [4]. These systematic effects were probed using cross reference measurements of carbon cluster ions, presented in Chapter 4, and were determined to lead to an error less than $10^{-9} \times m_{diff}$, where m_{diff} is in atomic mass units. Given that the mass difference for $^{78}Kr^{+}$ and $^{78}Se^{+}$ is on the order of $\sim 10^{-3}$ u, it is evident that mass-dependent systematic effects can be neglected in this measurement.

Systematic effects due to nonlinear magnetic field fluctuations also lead to an error much less than the statistical uncertainty. For measurements with a similar time period, ∼1 hour for an individual cyclotron frequency ratio, magnetic field fluctuations have been determined to lead to a systematic error well below 1×10^{-9} [33].

The purity of ion samples in the trap was also carefully examined, since the presence of residual contaminant ions during the measurement could result in frequency shifts proportional to the total number of trapped ions [4]. An analysis [1] was performed in which only a specific number of detected ions was considered for an individual cyclotron frequency measurement. Then the cyclotron frequency measurements, each with only events with a specific number of detected ions, were compared. This analysis did not reveal any correlation between the number of detected ions and the measured cyclotron frequency, which indicates that contamination is negligible. Moreover, to confirm the purity of the $^{78}Kr^{+}$ and $^{78}Se^{+}$ samples, a dipole rf electric field was set at the respective reduced cyclotron frequency to drive the desired ion species out of the trap. Then it was verified that no ions were detected on the MCP, i.e. that there were no contaminant ions present. Nonetheless as an additional safeguard, events with more than five detected ions were not considered for the measurement. With the detector efficiency of ∼80%, this corresponds to a limit of no more than six

simultaneously trapped ions. This limit eliminated the occasional event with large number of ions, but it did not significantly affect the statistics of the measurement since the vast majority of events had five or fewer detected ions.

Finally, the collection of cyclotron frequency ratios, shown in Fig. 6.2 (b), has a Birge ratio [77] of 1.05(5), which indicates that systematic effects are negligible and that the fluctuations in the data are purely statistical.

6.3 Determination of the ^{78}Kr Q value

The measured cyclotron frequency ratio of ^{78}Se and ^{78}Kr ions, $\nu_c(^{78}\mathrm{Se}^+)/\nu_c(^{78}\mathrm{Kr}^+)$, was used in the first direct determination of the ^{78}Kr double-electron capture Q value. Since the first-electron binding energy is negligible for the obtained precision, $Q_{\epsilon\epsilon}$ can simply be written as the difference in masses of the mother and daughter ions

$$Q_{\epsilon\epsilon} = [m(^{78}\mathrm{Kr}^+) - m(^{78}\mathrm{Se}^+)]c^2. \tag{6.1}$$

Factoring out the mass of $^{78}\mathrm{Se}^+$ and using the fact that the mass ratio is the inverse cyclotron frequency ratio yields an equivalent expression for $Q_{\epsilon\epsilon}$:

$$Q_{\epsilon\epsilon} = m(^{78}\mathrm{Se}^+)\left[\frac{\nu_c(^{78}\mathrm{Se}^+)}{\nu_c(^{78}\mathrm{Kr}^+)} - 1\right]c^2. \tag{6.2}$$

Using the measured cyclotron frequency ratio and the 2012 AME value of the atomic mass of ^{78}Se [7] (less the well known electron mass) yields an improved determination of the double electron capture Q value: $Q_{\epsilon\epsilon}$ = 2 847.75(27) keV. As illustrated in Fig. 6.3, the LEBIT value of $Q_{\epsilon\epsilon}$ is 1.4 keV greater than the value in the 2012 AME, and the uncertainty has

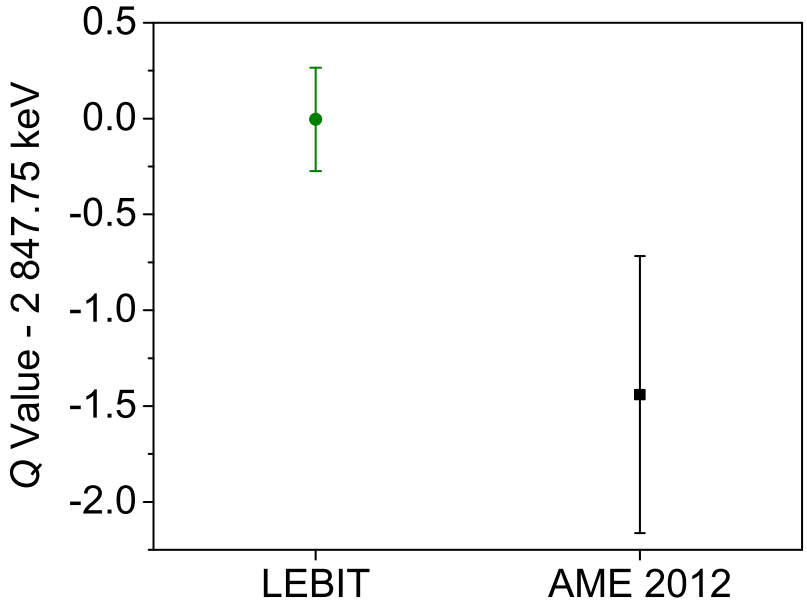

Figure 6.3: Comparison of the LEBIT Q value of double-electron capture in ^{78}Kr with that of the most recent Atomic Mass Evaluation.

been reduced by a factor of three.

6.4 Impact on the potential of ^{78}Kr as a neutrinoless double electron capture candidate

The possibility of 0νECEC resonance enhancement in ^{78}Kr to known excited states of ^{78}Se was investigated using the LEBIT determination of $Q_{\epsilon\epsilon}$. The degeneracy parameters for three different double electron captures to the identified 2^+ excited state are shown in Figure 6.4 and are listed in Table 6.1. The electron orbitals of these captures reflect that the spin must change by two units and that the parity should not change to avoid suppression. To calculate the degeneracy parameters the LEBIT Q value, the 2838.49 (7) keV [26] energy of the nuclear excited state, and the electron binding energies [82] were used. In order to determine B_{2h}, the two individual electron binding energies were added, neglecting the

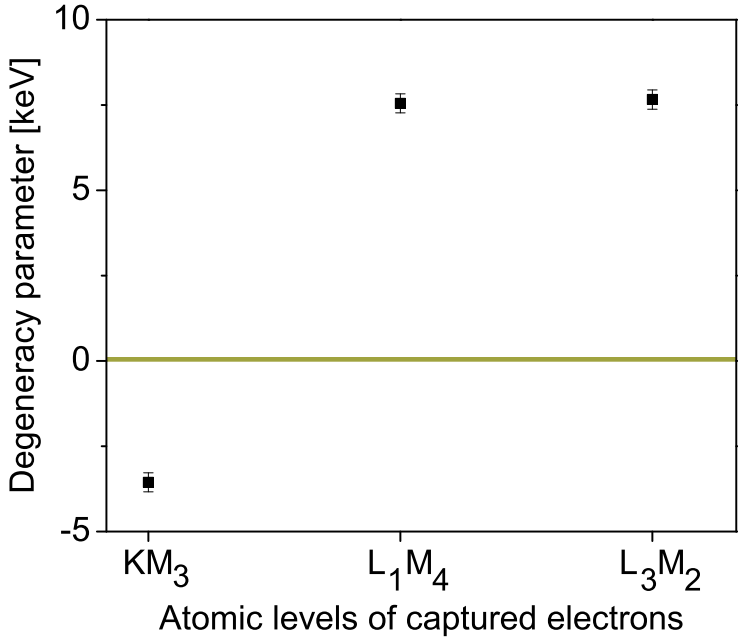

Figure 6.4: Degeneracy parameters for neutrinoless double-electron captures (0νECEC) to the 2838.49 (7) keV exited 2^+ state of ^{78}Se. These degeneracy parameters were calculated using the LEBIT determination of Q value. The gold bar indicates the sub-100 eV degeneracy required for significant enhancement. It is evident that the presented captures can be confidently excluded from candidates that could lead to resonantly enhanced 0νECEC

interaction of the two-electron hole. The interaction energy of two K shell electron holes for selenium is $\sim$ 500 eV, and the interaction energy is much less for outer electron holes [83]. Thus the B_{2h} approximation is reasonable given the large size of the degeneracy parameters compared to the interaction energy of the two electron holes. For the case of 0νECEC to the 2838.49 (7) keV state, K capture is energetically forbidden and would require a 3.6 keV greater Q value to be physically possible. Therefore, captures from outer electron orbitals must be considered. The degeneracy parameter for such captures, e.g. L_1M_4 and L_3M_2, however, is greater than 7 keV, quite far from the sub-100 eV degeneracy required for significant enhancement. Note that the uncertainty given for Δ considers the uncertainty of the Q value and of the nuclear excited state; it does not include the above-mentioned approximation used in the calculation of B_{2h}. Nonetheless, with the multiple-keV size of

Table 6.1: Parameters of neutrinoless double electron captures in ^{78}Kr to the 2838.49 (7) keV excited 2^+ state of ^{78}Se. Given in the columns are the atomic levels of the captured electrons, the binding energy of the two-electron hole, the degeneracy parameter, the radiative width, the resonance parameter, and the enhancement factor.

Orbitals	B_{2h}/keV	Δ/keV	Γ/eV	$F/(\text{keV}^{-1})$	EF
KM_3	12.82	-3.56 (28)			
L_1M_4	1.71	7.55 (28)	3.9	6.8×10^{-5}	1.2×10^5
L_3M_2	1.60	7.66 (28)	3.2	5.5×10^{-5}	9.6×10^4

the degeneracy parameters, it can already be soundly concluded that the 2^+ excited state of ^{78}Se is a poor candidate for resonant enhancement.

To show the effect that a large degeneracy parameter has on the decay rate of 0νECEC (see Equation 1.3), it is useful to calculate the resonance parameter, $F \equiv \Gamma/(\Delta^2 + \Gamma^2/4)$. The width of the two-electron-hole state dominates the nuclear radiative width, so to good approximation Γ can be calculated by summing the widths of the respective electron levels in Ref. [84]. The resonance parameters have been computed for L_1M_4 and L_3M_2 captures and are listed in Table 6.1. Also listed in Table 6.1 are the L_1M_4 and L_3M_2 enhancement factors, defined as the ratio of F for the considered transition to that of the nonresonant KK capture to the nuclear ground state. The large degeneracy parameters lead to small resonance parameters and weak enhancement factors $\sim 10^5$. Considering the maximum possible enhancement factors of $\sim 10^{12}$ for $\Delta = 0$, the calculated enhancement factors are miniscule.

In addition to the weak enhancement factors caused by the large degeneracy parameters, the decay rate of 0νECEC, given in Equation 1.3, is impeded by a small value of $\mathcal{M}$. The leptonic phase-space factor is suppressed since the captured electrons are from outer atomic orbitals, and the nuclear matrix element will be reduced by a factor of approximately 5.44 $\times 10^4$ [13] due to the hadronic recoil required for the $0^+ \rightarrow 2^+$ transition to proceed. This

combination together with the failure of the resonance enhancement condition causes the 2838.49 (7) keV 2^+ excited state in ^{78}Se to be a poor candidate for 0νECEC. The closest known excited states in ^{78}Se at 2754.46 (17) and 2864.12 (7) [26] are too far away to have any hope of resonance enhancement.

In conclusion, with the improved determination of the ^{78}Kr double-electron capture Q value, all known excited states in ^{78}Se can now be confidently excluded from possible candidates for resonantly enhanced 0νECEC.

Chapter 7

Summary and Outlook

This thesis work describes two LEBIT Penning trap measurements that impact neutrino physics. The first measurement, conducted in 2012, investigated the possibility of resonance enhancement of neutrinoless double electron capture in ^{78}Kr. In order to determine if a double electron capture transition were resonantly enhanced, the LEBIT Penning trap mass spectrometer was used to provide the first direct measurement of the ^{78}Kr double electron capture Q value. The measurement revealed a 1.4 keV increase in the Q value, a 2σ shift, and reduced the uncertainty by a factor of three. This increase in the Q value, however, was not sufficient to liberate double K shell electron capture, and thus ultimately moved double electron capture in ^{78}Kr further from resonance enhancement. With the improved determination of the Q value, ^{78}Kr can confidently be excluded as a viable candidate for neutrinoless double electron capture experiments.

In 2013, the first direct determination of the ^{48}Ca double beta decay Q value was conducted at the LEBIT facility. Accurate knowledge of this Q value is important for experiments that aim to detect neutrinoless double beta decay in ^{48}Ca. For the measurement, the Colutron ion source was operated in surface ionization mode to produce ions of $^{48}Ca^{+}$, and ions of $^{48}Ti^{+}$ were produced with the recently commissioned LEBIT laser ablation ion source. The resulting determination of the double beta Q value is 1.2 keV greater than the AME 2012 value, a change of 3σ, and the uncertainty has been reduced by a factor of

five. The two and zero neutrino phase space factors have been calculated with this improved determination of the Q value, which has reduced the uncertainty of each phase space factor by a factor of six. Moreover, the newly determined Q value in conjunction with the previous LEBIT determination of the atomic mass of ^{48}Ca yields an improved determination of the atomic mass of ^{48}Ti.

The ^{48}Ca double beta decay Q value illustrates the enhanced offline capabilities of the LEBIT facility with the recently commissioned laser ablation source (LAS). The design, fabrication, and implementation of LAS is the primary LEBIT technical development of this thesis work. LAS can produce ions for measurements of isotopes with direct scientific impact and can also be used to produce ions with essentially no mass uncertainty, e.g. carbon cluster ions. Cross reference measurements of carbon cluster ions provide the ideal opportunity to check LEBIT mass-dependent systematic effects. In 2013 LEBIT mass-dependent systematic effects were quantified by cross reference measurements of carbon cluster ions produced via laser ablation. The result of this study indicated that present systematic effects give rise to a relative error in mass determination that is less than 10^{-9}/u. Similar measurements can be performed in the future in order to optimize trap performance and reach an even higher level of mass accuracy.

BIBLIOGRAPHY

BIBLIOGRAPHY

[1] A. Kellerbauer, K. Blaum, G. Bollen, F. Herfurth, H.-J. Kluge, M. Kuckein, E. Sauvan, C. Scheidenberger, and L. Schweikhard. *Eur. Phys. J. D*, 22:53, 2003.

[2] A. Chaudhuri, M. Block, S. Eliseev, R. Ferrer, F. Herfurth, A. Martín, G. Marx, M. Mukherjee, C. Rauth, L. Schweikhard, and G. Vorobjev. *Eur. Phys. J. D*, 45:47, 2007.

[3] V.-V. Elomaa. PhD thesis, University of Jyväskylä, 2009.

[4] G. Bollen, S. Becker, H.-J. Kluge, M. König, R. B. Moore, T. Otto, H. Raimbault-Hartmann, G. Savard, L. Schweikhard, and H. Stolzenberg. *Nucl. Instrum. Methods Phys. Res., Sect. A*, 368:675, 1996.

[5] A.S. Barabash. *Phys. Part. Nuclei*, 42:613, 2011.

[6] A. P. Meshik, C. M. Hohenberg, O. V. Pravdivtseva, and Ya. S. Kapusta. *Phys. Rev. C*, 64:035205, 2001.

[7] G. Audi, M. Wang, A. H. Wapstra, F. G. Kondev, M. MacCormick, X. Xu, and B. Pfeiffer. *Chin. Phys. C*, 36:1603, 2012.

[8] A. de Gouvêa and P. Vogel. *Prog. Part. Nucl. Phys.*, 71:75, 2013.

[9] R. G. Winter. *Phys. Rev.*, 100:142, 1955.

[10] Z. Sujkowski and S. Wycech. *Phys. Rev. C*, 70:052501(R), 2004.

[11] J. Bernabeu, A. De Rujula, and C. Jarlskog. *Nucl. Phys. B*, 223:15, 1983.

[12] J. Suhonen. *Eur. Phys. J. A*, 48:51, 2012.

[13] V. S. Kolhinen, V.-V. Elomaa, T. Eronen, J. Hakala, A. Jokinen, M. Kortelainen, J. Suhonen, and J. Äystö. *Phys. Lett. B*, 684:17, 2010.

[14] B. J. Mount, M. Redshaw, and E. G. Myers. *Phys. Rev. C*, 81:032501(R), 2010.

[15] M. Goncharov, K. Blaum, M. Block, C. Droese, S. Eliseev, F. Herfurth, E. Minaya Ramirez, Yu. N. Novikov, L. Schweikhard, and K. Zuber. *Phys. Rev. C*, 84:028501, 2011.

[16] C. Smorra, T. Beyer, K. Blaum, M. Block, Ch. E. Düllmann, K. Eberhardt, M. Eibach, S. Eliseev, Sz. Nagy, W. Nörtershäuser, and D. Renisch. *Phys. Rev. C*, 85:027601, 2012.

[17] S. Eliseev, C. Roux, K. Blaum, M. Block, C. Droese, F. Herfurth, M. Kretzschmar, M. I. Krivoruchenko, E. Minaya Ramirez, Yu. N. Novikov, L. Schweikhard, V. M. Shabaev, F. Šimkovic, I. I. Tupitsyn, K. Zuber, and N. A. Zubova. *Phys. Rev. Lett.*, 107:152501, 2011.

[18] S. Rahaman, V.-V. Elomaa, T. Eronen, J. Hakala, A. Jokinen, A. Kankainen, J. Rissanen, J. Suhonen, C. Weber, and J. Äystö. *Phys. Rev. Lett.*, 103:042501, 2009.

[19] S. Eliseev, C. Roux, K. Blaum, M. Block, C. Droese, F. Herfurth, H.-J. Kluge, M. I. Krivoruchenko, Yu. N. Novikov, E. Minaya Ramirez, L. Schweikhard, V. M. Shabaev, F. Šimkovic, I. I. Tupitsyn, K. Zuber, and N. A. Zubova. *Phys. Rev. Lett.*, 106:052504, 2011.

[20] S. Eliseev, D. Nesterenko, K. Blaum, M. Block, C. Droese, F. Herfurth, E. Minaya Ramirez, Yu. N. Novikov, L. Schweikhard, and K. Zuber. *Phys. Rev. C*, 83:038501, 2011.

[21] C. Droese, K. Blaum, M. Block, S. Eliseev, F. Herfurth, E. Minaya Ramirez, Yu.N. Novikov, L. Schweikhard, V.M. Shabaev, I.I. Tupitsyn, S. Wycech, K. Zuber, and N.A. Zubova. *Nuc. Phys. A*, 875:1, 2012.

[22] D. A. Nesterenko, K. Blaum, M. Block, C. Droese, S. Eliseev, F. Herfurth, E. Minaya Ramirez, Yu. N. Novikov, L. Schweikhard, V. M. Shabaev, M. V. Smirnov, I. I. Tupitsyn, K. Zuber, and N. A. Zubova. *Phys. Rev. C*, 86:044313, 2012.

[23] S. Eliseev, M. Goncharov, K. Blaum, M. Block, C. Droese, F. Herfurth, E. Minaya Ramirez, Yu. N. Novikov, L. Schweikhard, V. M. Shabaev, I. I. Tupitsyn, K. Zuber, and N. A. Zubova. *Phys. Rev. C*, 84:012501(R), 2011.

[24] V. S. Kolhinen, T. Eronen, D. Gorelov, J. Hakala, A. Jokinen, A. Kankainen, J. Rissanen, J. Suhonen, and J. Äystö. *Phys. Lett. B*, 697:116, 2011.

[25] N. D. Scielzo, S. Caldwell, G. Savard, J. A. Clark, C. M. Deibel, J. Fallis, S. Gulick, D. Lascar, A. F. Levand, G. Li, J. Mintz, E. B. Norman, K. S. Sharma, M. Sternberg, T. Sun, and J. Van Schelt. *Phys. Rev. C*, 80:025501, 2009.

[26] Department of Physics, Center for Nuclear Studies, The George Washington University. Data Analysis Center: [http://www.nndc.bnl.gov]; status on January 2014.

[27] G. Audi, M. Wang, A.H. Wapstra, F.G. Kondev, M. MacCormick, X. Xu, and B. Pfeiffer. *Chin. Physics C*, 36:1287, 2012.

[28] International Atomic Energy Agency. *Database of Prompt Gamma Rays from Slow Neutron Capture for Elemental Analysis: Neutron-capture Prompt-gamma Activation Analysis*. International Atomic Energy Agency, 2007.

[29] G. Engler, R. E. Chrien, and H.I. Liou. *Nuc. Phys. A*, 372:125, 1981.

[30] A. S. Barabash. *Phys. Rev. C*, 81:035501, 2010.

[31] V. S. Kolhinen, T. Eronen, D. Gorelov, J. Hakala, A. Jokinen, A. Kankainen, I. D. Moore, J. Rissanen, A. Saastamoinen, J. Suhonen, and J. Äystö. *Phys. Rev. C*, 82:022501, 2010.

[32] S. Rahaman, V.-V. Elomaa, T. Eronen, J. Hakala, A. Jokinen, J. Julin, A. Kankainen, A. Saastamoinen, J. Suhonen, C. Weber, and J. Äystö. *Phys. Lett. B*, 662:111, 2008.

[33] D. L. Lincoln, J. D. Holt, G. Bollen, M. Brodeur, S. Bustabad, J. Engel, S. J. Novario, M. Redshaw, R. Ringle, and S. Schwarz. *Phys. Rev. Lett.*, 110:012501, 2013.

[34] S. Rahaman, V.-V. Elomaa, T. Eronen, J. Hakala, A. Jokinen, A. Kankainen, J. Rissanen, J. Suhonen, C. Weber, and J. Äystö. *Phys. Lett. B*, 703:412, 2011.

[35] M. Redshaw, B. J. Mount, E. G. Myers, and F. T. Avignone. *Phys. Rev. Lett.*, 102:212502, 2009.

[36] G. Douysset, T. Fritioff, C. Carlberg, I. Bergström, and M. Björkhage. *Phys. Rev. Lett.*, 86:4259, 2001.

[37] D. Fink, J. Barea, D. Beck, K. Blaum, Ch. Böhm, Ch. Borgmann, M. Breitenfeldt, F. Herfurth, A. Herlert, J. Kotila, M. Kowalska, S. Kreim, D. Lunney, S. Naimi, M. Rosenbusch, S. Schwarz, L. Schweikhard, F. Šimkovic, J. Stanja, and K. Zuber. *Phys. Rev. Lett.*, 108:062502, 2012.

[38] A. Balysh, A. De Silva, V. I. Lebedev, K. Lou, M. K. Moe, M. A. Nelson, A. Piepke, A. Pronskiy, M. A. Vient, and P. Vogel. *Phys. Rev. Lett.*, 77:5186, 1996.

[39] V.B. Brudanin, N.I. Rukhadze, Ch. Brianon, V.G. Egorov, V.E. Kovalenko, A. Kovalik, A.V. Salamatin, I. Štekl, V.V. Tsoupko-Sitnikov, Ts. Vylov, and P. Čermák. *Phys. Lett. B*, 495:63, 2000.

[40] R. L. Flack (Nemo-3 Collaboration). *J. Phys. Conf. Ser.*, 136:022032, 2008.

[41] R. Arnold, C. Augier, J. Baker, A. Barabash, D. Blum, V. Brudanin, A.J. Caffrey, J.E. Campagne, E. Caurier, D. Dassié, V. Egorov, T. Filipova, R. Gurriaran, J.L. Guyonnet, F. Hubert, Ph. Hubert, S. Jullian, I. Kisel, O. Kochetov, V.N. Kornoukhov, V. Kovalenko, D. Lalanne, F. Laplanche, F. Leccia, I. Linck, C. Longuemare, Ch. Marquet, F. Mauger, H.W. Nicholson, I. Pilugin, F. Piquemal, J-L. Reyss, X. Sarazin, F. Scheibling, J. Suhonen, C.S. Sutton, G. Szklarz, V. Timkin, R. Torres, V.I. Tretyak, V. Umatov, I. Vanyushin, A. Vareille, Yu. Vasilyev, and Ts. Vylov. *Nuc. Phys. A*, 658:299, 1999.

[42] A. A. Kwiatkowski, T. Brunner, J. D. Holt, A. Chaudhuri, U. Chowdhury, M. Eibach, J. Engel, A. T. Gallant, A. Grossheim, M. Horoi, A. Lennarz, T. D. Macdonald, M. R. Pearson, B. E. Schultz, M. C. Simon, R. A. Senkov, V. V. Simon, K. Zuber, and J. Dilling. *Phys. Rev. C*, 89:045502, 2014.

[43] M. Jerkins, I. Chavez, U. Even, and M. G. Raizen. *Phys. Rev. A*, 82:033414, 2010.

[44] I. Ogawa, T. Kishimoto, S. Umehara, G. Ito, K. Yasuda, H. Kakubata, M. Miyashita, K. Takubo, K. Matsuoka, M. Nomachi, M. Saka, K. Seki, K. Fushimi, R. Hazama, H. Ohsumi, K. Okada, Y. Tamagawa, T. Jinno, N. Fujiwara, and S. Yoshida (Candles Collaboration). *J. Phys. Conf. Ser.*, 375:042018, 2012.

[45] S. Yoshida, T. Kishimoto, I. Ogawa, R. Hazama, S. Umehara, K. Matsuoka, D. Yokoyama, K. Ichihara, and Y. Tatewaki. *Nucl. Instrum. Methods Phys. Res. Sect. A*, 601:282, 2009.

[46] S. Umehara, T. Kishimoto, M. Nomachi, S. Yoshida, S. Ajimura, K. Suzuki, K. Ichimura, K. Matsuoka, N. Nakatani, G. Ito, H. Kakubata, M. Saka, W. Wang, J. Takemoto, W. Chan, M. Doihara, Y. Tamagawa, I. Ogawa, S. Ueno, S. Maeda, A. Yamamoto, S. Tomita, G. Fujita, A. Kawamura, T. Harada, K. Fushimi, R. Hazama, H. Ohsumi, and K. Okada. *AIP Conf. Proc.*, 1533:115, 2013.

[47] Yu.G. Zdesenko, F.T. Avignone III, V.B. Brudanin, F.A. Danevich, V.V. Kobychev, B.N. Kropivyansky, S.S. Nagorny, V.I. Tretyak, and Ts. Vylov. *Astropart. Phys.*, 23:249, 2005.

[48] M. Redshaw, G. Bollen, M. Brodeur, S. Bustabad, D. L. Lincoln, S. J. Novario, R. Ringle, and S. Schwarz. *Phys. Rev. C*, 86:041306, 2012.

[49] G. Audi, A.H. Wapstra, and C. Thibault. *Nucl. Phys. A*, 729:337, 2003.

[50] G. Audi and M. Wang (private communication).

[51] D.J. Morrissey, B.M. Sherrill, M. Steiner, A. Stolz, and I. Wiedenhoever. *Nucl. Instrum. Methods Phys. Res. Sect. B*, 204:90, 2003.

[52] G. Savard. *J. Phys. Conf. Ser.*, 312:052004, 2011.

[53] A. E. Gehring. PhD thesis, Michigan State University, 2013.

[54] C. Smorra. PhD thesis, Johannes Gutenberg-Universität Mainz, 2008.

[55] A. M. Klose. PhD thesis, Michigan State University, 2013.

[56] S. Schwarz, G. Bollen, D. Lawton, A. Neudert, R. Ringle, P. Schury, and T. Sun. *Nucl. Instrum. Methods Phys. Res., Sect. B*, 204:474, 2003.

[57] T. Sun. PhD thesis, Michigan State University, 2006.

[58] R. Ringle, G. Bollen, A. Prinke, J. Savory, P. Schury, S. Schwarz, and T. Sun. *Nucl. Instrum. Methods Phys. Res., Sect. A*, 604:536, 2009.

[59] R. Ringle. PhD thesis, Michigan State University, 2006.

[60] M. Kretzschmar. *Eur. J. Phys.*, 12:240, 1991.

[61] K. Blaum. *Phys. Rep.*, 425:1, 2006.

[62] L. S. Brown and G. Gabrielse. *Phys. Rev. A*, 25:2423, 1982.

[63] G. Gabrielse. *Int. J. Mass Spectrom.*, 279:107, 2009.

[64] R. Ringle, G. Bollen, A. Prinke, J. Savory, P. Schury, S. Schwarz, and T. Sun. *Int. J. Mass Spectrom.*, 263:38, 2007.

[65] G. Gräff, H. Kalinowsky, and J. Traut. *Z. Phys. A*, 297:35, 1980.

[66] M. König, G. Bollen, H.-J. Kluge, T. Otto, and J. Szerypo. *Int. J. Mass Spectrom. Ion Processes*, 142:95, 1995.

[67] G. Bollen, H.-J. Kluge, T. Otto, G. Savard, and H. Stolzenberg. *Nucl. Instrum. Methods B*, 70:490, 1992.

[68] M. Kretzschmar. *Int. J. Mass Spectrom.*, 264:122, 2007.

[69] S. George, K. Blaum, F. Herfurth, A. Herlert, M. Kretzschmar, S. Nagy, S. Schwarz, L. Schweikhard, and C. Yazidjian. *Int. J. Mass Spectrom.*, 264:110, 2007.

[70] F. S. Breech and L. Cross. *Appl. Spectrosc*, 16:59, 1962.

[71] D. A. Davies. PhD thesis, Michigan State University, 2006.

[72] R. E. Russo, X. L. Mao, C. Liu, and J. Gonzalez. *J. Anal. At. Spectrom.*, 19:1084, 2004.

[73] C. Smorra, K. Blaum, K. Eberhardt, M. Eibach, J. Ketelaer, J. Ketter, K. Knuth, and Sz. Nagy. 42:154028, 2009.

[74] J. D. Jackson. *Classical Electrodynamics*. JWS, Inc., 1998.

[75] Refractive Index Database: [http://refractiveindex.info]; status on March 2014.

[76] A. E. Siegman. *Lasers*. Univ. Science Books, 1986.

[77] R. T. Birge. *Phys. Rev.*, 40:207, 1932.

[78] S. Bustabad, G. Bollen, M. Brodeur, D. L. Lincoln, S. J. Novario, M. Redshaw, R. Ringle, S. Schwarz, and A. A. Valverde. *Phys. Rev. C*, 88:022501, 2013.

[79] J. Suhonen and O. Civitarese. *Phys. Rep.*, 300:123, 1998.

[80] J.F.A.G. Ruyl, J.B.M. De Haas, P.M. Endt, and L. Zybert. *Nuc. Phys. A*, 419:439, 1984.

[81] S. Naimi, G. Audi, D. Beck, K. Blaum, Ch. Böhm, Ch. Borgmann, M. Breitenfeldt, S. George, F. Herfurth, A. Herlert, A. Kellerbauer, M. Kowalska, D. Lunney, E. Minaya Ramirez, D. Neidherr, M. Rosenbusch, L. Schweikhard, R. N. Wolf, and K. Zuber. *Phys. Rev. C*, 86:014325, 2012.

[82] F. P. Larkins. *At. Data Nucl. Data Tables*, 20:311, 1977.

[83] M. I. Krivoruchenko, F. Šimkovic, D. Frekers, and A. Faessler. *Nucl. Phys. A*, 859:140, 2011.

[84] J. L. Campbell and T. Papp. *At. Data Nucl. Data Tables*, 77:1, 2001.